

# REMOTE SENSING OF ENVIRONMENT

Estimating fractional cover of photosynthetic vegetation, non-photosynthetic vegetation and bare soil in the Australian tropical savanna region upscaling the EO-1 Hyperion and MODIS sensors

## Abstract

Quantitative estimation of fractional cover of photosynthetic vegetation (fPV), non-photosynthetic vegetation (fNPV) and bare soil (fBS) is critical for natural resource management and for modeling carbon dynamics. Accurate estimation of fractional cover is especially important for monitoring and modeling savanna systems, subject to highly seasonal rainfall and drought, grazing by domestic and native animals, and frequent burning. This paper describes a method for resolving fPV, fNPV and fBS across the ~2 million km<sup>2</sup> Australian tropical savanna zone with hyperspectral and multispectral imagery. A spectral library compiled from field campaigns in 2005 and 2006, together with three EO-1 Hyperion scenes acquired during the 2005 growing season were used to explore the spectral response space for fPV, fNPV and fBS. A linear unmixing approach was developed using the Normalized Difference Vegetation Index (NDVI) and the Cellulose Absorption Index (CAI). Translation of this approach to MODerate resolution Imaging Spectroradiometer (MODIS) scale was assessed by comparing multiple linear regression models of NDVI and CAI with a range of indices based on the seven MODIS bands in the visible and

shortwave infrared region (SWIR) using synthesized MODIS surface reflectance data on the same dates as the Hyperion acquisitions. The best resulting model, which used NDVI and the simple ratio of MODIS bands 7 and 6 (SWIR3/SWIR2), was used to generate a time series of fractional cover from 16 day MODIS nadir bidirectional reflectance distribution function-adjusted reflectance (NBAR) data from 2000–2006. The results obtained with MODIS NBAR were validated against grass curing measurement at ten sites with good agreement at six sites, but some underestimation of fNPV proportions at four other sites due to substantial sub-pixel heterogeneity. The model was also compared with remote sensing measurements of fire scars and showed a good matching in the spatio-temporal patterns of grass senescence and posterior burning. The fractional cover profiles for major grassland cover types showed significant differences in relative proportions of fPV, fNPV and fBS, as well as large intra-annual seasonal variation in response to monsoonal rainfall gradients and soil type. The methodology proposed here can be applied to other mixed tree-grass ecosystems across the world.

*Crown Copyright © 2009 Published by Elsevier Inc. All rights reserved.*

## 1. Introduction

Savannas are mixed tree-grass ecosystems, often including patches of forest and treeless grassland, that occupy large areas of tropical and temperate regions, particularly in Australia, Africa and South America (Mistry, 2000). In the tropical savannas that dominate the northern third of Australia, ecosystem and carbon dynamics are primarily controlled by seasonal monsoon rains (Chen et al., 2003; Leuning et al., 2005). The water balance and hydrodynamics of these systems are intimately related to the landscape and patch-scale vegetation structure (Bastin et al., 2003). The ability of the landscape to capture rainfall is a key ecosystem property. Recent research has linked landscape function to the 'leakiness' of such systems – the extent to which they capture rainfall or lose it through surface runoff (e.g., Ludwig et al., 2002, 2004, 2005). The leakiness is highly dependent upon the proportion of the surface occupied by vegetation and bare soil. The water balance in these systems is then controlled by transpiration and evaporation through the proportions of photosynthetically active vegetation (fPV) and non-photosynthetically active vegetation (fNPV) and bare soil (fBS) (Scanlon et al., 2005), as well as the mix of trees and grass accessing water at different depths (e.g., Leuning et al., 2005).

From a functional perspective, vegetation can be classified as photosynthetic (green leaves) and non-photosynthetic (aboveground dead biomass, litter and wood). The amount of photosynthetic and non-photosynthetic biomass

determine key ecosystem features like the rate of carbon and nutrient uptake, the exchange of latent and sensible heat between the surface and the atmosphere, and surface albedo. Non-photosynthetic vegetation also plays a key role in determining fire frequency and intensity, and in controlling wind and water erosion (McTainsh et al., 2006). In savannas and grasslands, photosynthetic and non-photosynthetic vegetation vary seasonally roughly following precipitation patterns. In northern Australia, for instance, vegetation photosynthesis, growth and canopy development occurs during the 'wet-season' from November to March. During the dry period, vegetation can maintain photosynthesis if it has access to water (e.g., deep-rooted perennial trees); otherwise it senesces, becomes non-photosynthetic and dries. The fire season begins as soon as the monsoon finishes (April) and peaks towards the end of the dry season (July–September), when the herbaceous layer has accumulated a large amount of dry biomass and litter moisture is minimum. Fires play an important role in the structure and function of tropical and temperate savannas including carbon cycling (Beringer et al., 2007; Grace et al., 2006) species composition (D'Odorico et al., 2006), and emission of aerosols and trace gases (Ji and Stocker, 2002). Developing tools that allow monitoring of vegetation in space and time is a key step needed to improved management of savannas.

Remote sensing is an important tool for estimating the fractional cover of vegetation as a key descriptor of ecosystem

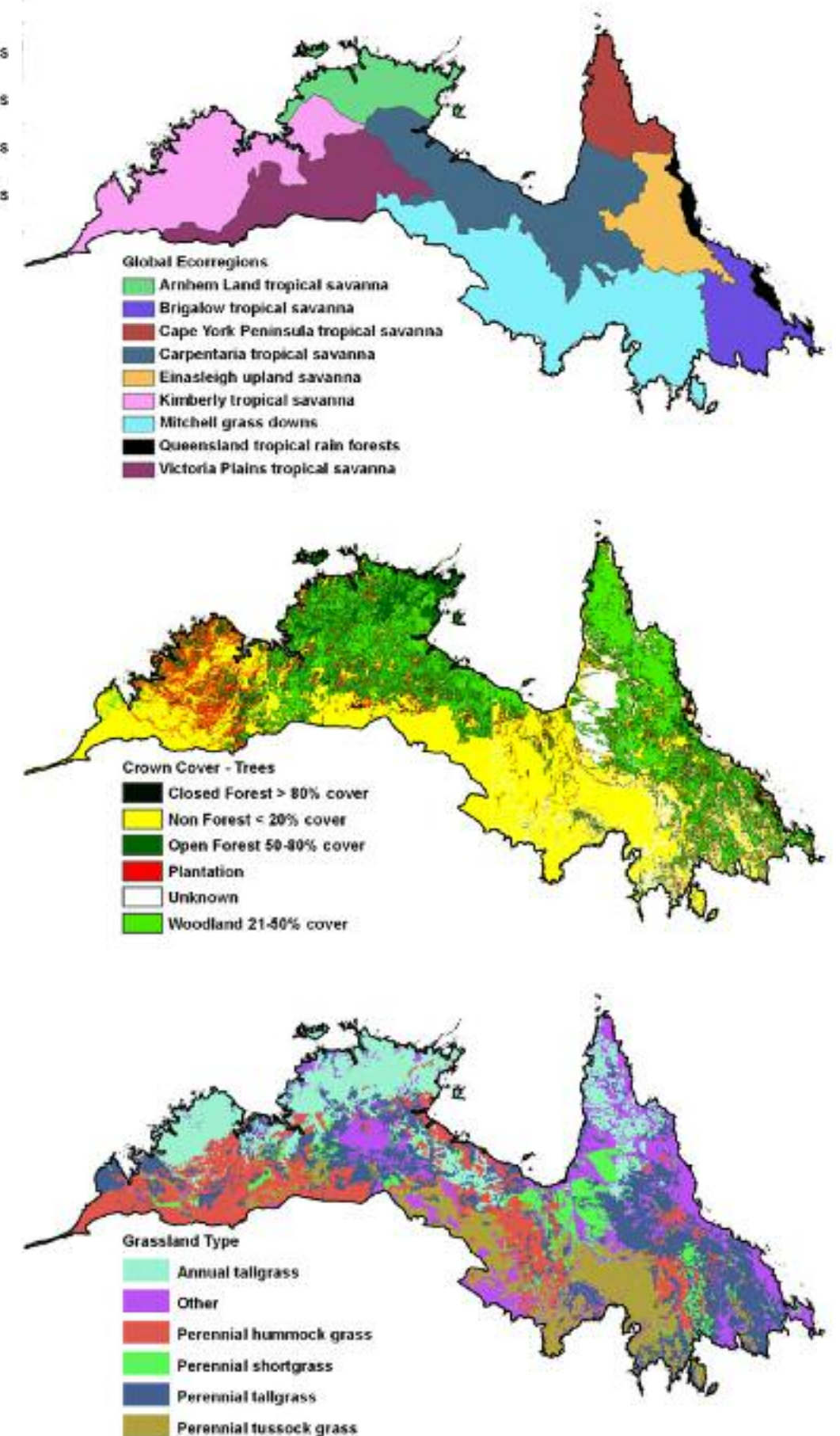
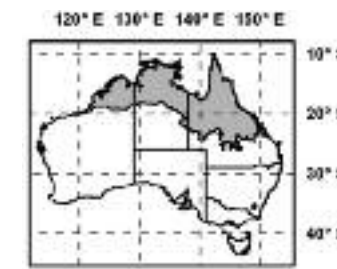


FIGURE 1 a) Australian tropical savanna zone defined by Fox et al. (2001) compared with the global ecoregions (Olson et al., 2001) showing inclusion of Mitchell grassland and the partial inclusion of the Brigalow region. b) Tree canopy cover for the Australian tropical savanna zone (NFI, 2003). c) Grassland type based on species and growth form for the Australian tropical savanna zone (derived from grassland mapping reported in (Hill et al., 2005) based on (Fox et al., 2001). 930

function (e.g., Asner and Heidebrecht, 2003; Asner et al., 2005b). Two complementary spectral properties of vegetation have been used in remote sensing analyses to discriminate green and dry vegetation from soils. Firstly, the Normalized Difference Vegetation Index (NDVI) utilizes absorption by chlorophyll in the red wavelength and scattering by cellulose in near infra-red wavelengths to distinguish green vegetation (Tucker, 1979; Ustin et al., 2004). Secondly, the Cellulose Absorption Index (CAI) is based on the absorption feature in the 2000 to 2200 nm region due to cellulose and lignin in plant biomass (Nagler et al., 2003). Absorption at these wavelengths is greatest in dry vegetation and absent from soil or green vegetation reflectance spectra (Nagler et al., 2000). The CAI calculates the ratio of reflectance at 2100 nm and 2000–2200 nm to resolve non-photosynthetic vegetation. Asner and Lobell (2000) developed a technique based on linear unmixing of the spectral features in the shortwave infrared (SWIR) bands affected by cellulose and lignin and applied it to mapping fPV, fNPV, and fBS using the Airborne Visible/Infrared Imaging Spectrometer (AVIRIS) sensor in semiarid shrublands, tropical forests and along a vegetation gradient in Hawaii (Asner et al., 2003, 2004, 2005a). Similar approaches have been used to map forest fuel and post-fire condition using AVIRIS (Jia et al., 2006) and to monitor the spatial distribution of degradation and desertification (Asner et al., 2003; Huete et al., 2003). An alternative method proposed by Daughtry (2001)



to map tillage practices in agricultural areas showed that fPV (healthy crops) was separated from fNPV (dry crops and crop residues in conservation tillage) and fBS (conventional tillage) using NDVI. At the same time, the Cellulose Absorption Index (CAI) was able to separate fNPV from fBS. Daughtry et al. (2006) applied this idea for mapping tillage practices with EO-1 Hyperion data in a test site in central Iowa, USA.

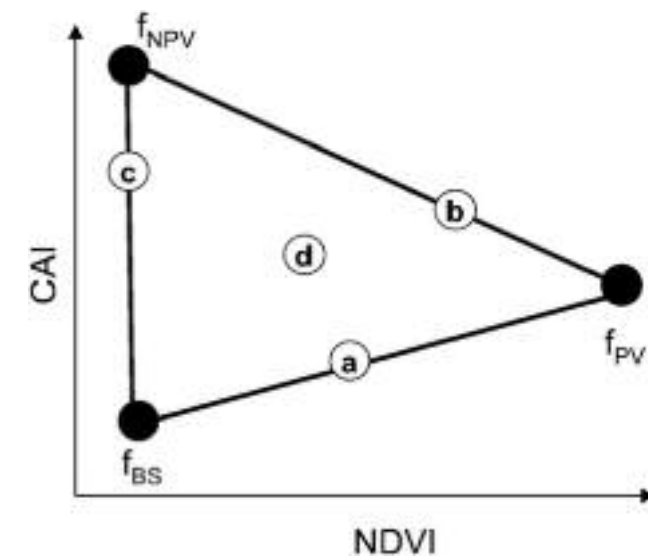
Whilst fractional cover of fPV, fNPV and fBS can be estimated with hyperspectral sensors with good results, this becomes more difficult with multi-spectral sensors since there is limited sensitivity, and nonideal band widths and locations in the SWIR, where discrimination of soils and senescent/dry vegetation is most effective (Asner and Lobell, 2000). Previous attempts to map vegetation fractional cover with AVHRR and MODIS over large areas have focused on the discrimination of trees and grasses (sometimes referred to as perennial and annual vegetation (Lu et al., 2003) or recurrent and persistent vegetation (Donohue et al., 2008a,b). These studies decomposed the temporal variations in vegetation greenness into a slow varying component (perennial, or trees) and a rapid varying component (annual, or herbaceous) (e.g., Berry and Roderick, 2002; Donohue et al., 2008b; Lu et al., 2003) and have been used to produce a 27 year continental time series of evergreen vegetative cover from AVHRR (Donohue et al., 2008b). These studies, however, do not provide a means for distinguishing between fPV and fNPV. Marsett et al. (2006) have developed the Soil Adjusted Total Vegetation Index (SATVI), an index that incorporates reflectance in the red, SWIR1 and SWIR2 bands together with the soil line concept from the Soil Adjusted Vegetation Index (Huete, 1988), to estimate total

fractional vegetation cover i.e. green plus senescent versus bare soil. Multiple endmember spectral mixture analysis (MESMA) has been used for resolving vegetation fractional cover with LANDSAT (e.g., Numata et al., 2007) and ASTER (e.g., Gill and Phinn, 2009) with modest results. Okin (2007) applied a similar approach for mapping fractional cover over large areas using MODIS imagery. He argued that the reflectance spectra of soil and non photosynthetic vegetation are not dissimilar enough in MODIS bands as to be quantitatively estimated and consequently he developed a relative spectral mixture analysis, i.e., the quantities are estimated relative to an initial date selected arbitrarily. Here we test this assumption in the Australian savannas context using a simpler, empirical approach. The aim of this study was to quantitatively estimate fractional cover of fPV, fNPV and fBS over Australia's tropical savanna region using an upscaling procedure between Hyperion and MODIS surface reflectance. This study is divided into two sections. First, data collected in the field and from EO-1 Hyperion imagery are used to i) explore the spectral features of vegetation and their variability in space and time for a single 185 kmswath the tropical savanna zone near Darwin; and ii) develop a linear unmixing technique based on the NDVI and the CAI. Second, EO-1 Hyperion, daily MODIS surface reflectance and MODIS 16-day composite nadir BRDF-adjusted reflectance are used to i) develop a scaling relationship between NDVI and CAI from Hyperion resampled to MODIS resolution, and NDVI and SWIR indices as CAI surrogates from MODIS surface reflectance; ii) produce a MODISbased time series of fractional cover of fPV, fNPV and fBS at 1000 m resolution for the tropical savanna region of Australia;

and iii) validate both Hyperion and MODIS-based fractional cover against fire scar data and data from sites used to estimate grassland curing. **2. The tropical savanna zone** The Australian tropical savanna zone as described by Fox et al. (2001) includes large areas of tussock grassland on black soil plains of the Mitchell Grass Downs. This was chosen as our broad regional definition of the "Australian savanna zone" because it captures a continuum from small pockets of rainforest to open grassland influenced by the tropical monsoon, subject to extensive grazing and supporting a large cattle population, and represents the tropical zone where fractional cover is extremely important as an influence on rainfall capture and carbon dynamics (Hill et al., 2006a; Hill et al., 2006b). The area of the Australian savannas as defined here is almost 2 million km<sup>2</sup> (26% of the Australian land area). The relationship between this zone

(Fox et al., 2001) and the global ecoregion definitions (Olson et al., 2001) is shown in Fig. 1a. The distribution of tree cover and grassland types is shown in Fig. 1b and c respectively. Most of the region is either true open savanna or grassland since tree cover is sparse. Hence, spectral signatures are dominated by understory grassland and soil except where tree canopy cover is N50% (e.g., Hill et al., 2006a). **3. Conceptual model** Based on Daughtry et al. (2006) it was hypothesized that in any canopy, fractions of f<sub>PV</sub>, f<sub>NPV</sub> and f<sub>BS</sub> can be resolved by using the 929 complementary indices NDVI and CAI. In a scatterplot of CAI versus NDVI (referred hereafter to as the NDVI-CAI plane) reflectance spectra form a triangle; green vegetation having a high NDVI and intermediate values of CAI; dry vegetation and litter having low NDVI and high CAI; and bare soil having both low NDVI and low CAI values (Fig. 2). Any given mixture of f<sub>PV</sub>, f<sub>NPV</sub> and f<sub>BS</sub> should be located within this triangle. If the position of

**FIGURE 2** The conceptual approach for quantifying vegetation fractional cover using hyperspectral data. A collection of reflectance spectra acquired in a savanna during a growing season will form a triangle in the space defined by the Normalized Difference Vegetation Index (NDVI) and the Cellulose Absorption Index (CAI). "Pure" f<sub>PV</sub>, f<sub>NPV</sub> and f<sub>BS</sub> reflectance spectra (called endmembers) will be located in the vertices of the triangle (black circles), while reflectance spectra of mixtures of the three endmembers will be located within the triangle.



the "pure pixels" (endmembers) are known, the relative abundance of each fractional cover type should be resolved by linear unmixing. In the hypothetical example shown in Fig. 2, (a) is composed by f<sub>PV</sub> (50%) and f<sub>BS</sub> (50%), (b) contains f<sub>PV</sub> (67%) and f<sub>NPV</sub> (33%), (c) contains f<sub>NPV</sub> (67%) and f<sub>BS</sub> (33%), and (d) is composed by a mixture of 33% of each of the 3 endmembers. We then hypothesized that surrogates for the CAI could be found among various vegetation indices calculated using the visible and/or SWIR bands (after Marsett et al., 2006), and that these could be used along with NDVI to create an effective dataspace for unmixing f<sub>PV</sub>, f<sub>NPV</sub> and f<sub>BS</sub> using a time series of MODIS surface reflectance.

## 4. Data

**4.1. Field spectral measurements** The reflectance spectra of tree leaves, grasses and soils were collected at 7 sites in the Northern Territory (Fig. 3), Australia with a portable spectrometer (Analytical Spectral Devices Inc., Boulder, CO, USA) at 1.4 nm intervals in the visible and near-infrared (400–1100 nm) and at 2.2 nm intervals in the near-infrared

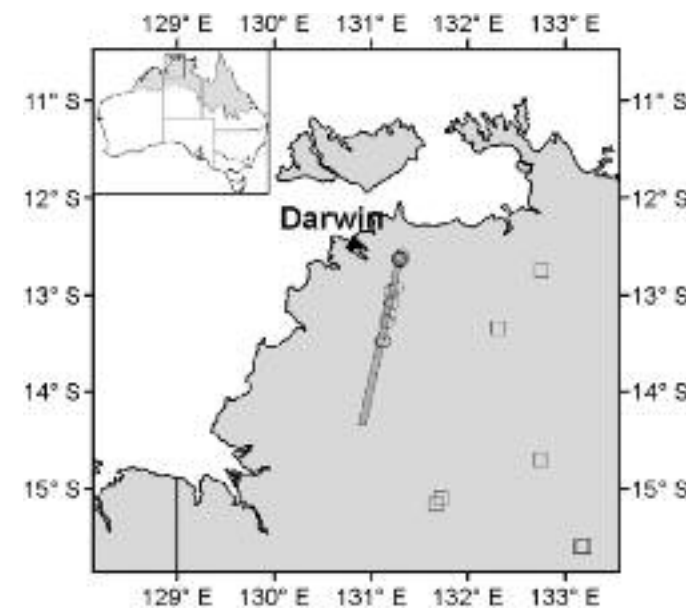
to shortwave infrared (1100–2500 nm). Tissue hemispherical reflectance and transmittance were measured. Tree leaves were removed intact on branches from the canopy and measured with the ASD in the same orientation as in the canopy at a distance of approximately 5 cm. Grasses containing different proportions of green leaves, dry leaves and standing dead leaves were measured vertically at a distance of 1 m. Bare soil patches were located or generated by removing all vegetation and reflectance was measured at a vertical height of 1 m. A total of 72 reflectance spectra from tree leaves, 53 from grasses and 30 from bare soil were collected. Measurements were taken between 10 am and 4 pm in July 2006, with typical 'dry-season' conditions (i.e., clear sky). The NDVI and CAI were calculated for each spectrum as follows:

$$NDVI = \frac{\rho_{NIR} - \rho_{RED}}{\rho_{NIR} + \rho_{RED}} \quad (1)$$

$$CAI = \frac{\rho_{2.0} - \rho_{2.1} + \rho_{2.2} - \rho_{2.3}}{\rho_{2.0} + \rho_{2.1}} \cdot 10 \quad (2)$$

where wavelength ranges of  $\rho_{NIR}$ ,  $\rho_{RED}$ ,  $\rho_{2.0}$ ,  $\rho_{2.1}$  and  $\rho_{2.2}$  are given in Table 1. The CAI normally ranges between -0.03 to 0.06. It is multiplied here by a

**FIGURE 3** Location of the 7 field sites where reflectance spectra were collected and used for calibration (squares, July 2006) and 12 sites used for validation (circles, May and August 2005). The location of the EO-1 images is also shown in dark grey strip.



factor of ten to ensure that it has a similar order of magnitude as the NDVI, which normally ranges from 0 to 0.8, what facilitates some of the analyses outlined in Section 5.

## 4.2. Satellite data

### 4.2.1. EO-1 Hyperion

EO-1 Hyperion images were acquired over the same location near Darwin in the Northern Territory during 2005 on April 30th, July 3rd and September 5th, corresponding to the beginning, middle and end of the dry season. Hyperion data have a 30 m pixel resolution and a swath 185 km long and 7.5 km wide. Hyperion samples the 400–2400 nm region of the electromagnetic spectrum at intervals of 10 nm yielding 242 bands. The three images were radiometrically calibrated using gain/bias information provided in the image headers and atmospherically corrected using ACORN 5.1 following the procedures developed by Apan and Held (2002), Apan et al. (2004), Datt et al. (2003), Jupp et al. (2002). Images were geometrically rectified using ground control points based on the Landsat 7 Picture Mosaic of Australia (Geoscience Australia, [http://www.ga.gov.au/acres/prod\\_ser/l7\\_picmosaic.jsp](http://www.ga.gov.au/acres/prod_ser/l7_picmosaic.jsp)). The April and July Hyperion images were cloud free. However, the September image showed increasing cloud contamination at its southernmost end and these were manually masked from the image (including

shadows). The vegetation indices, NDVI and CAI, were calculated using Eqs. (1) and (2) at wavelengths reported in Table 1.

### 4.2.2. Daily MODIS data

MODIS-Terra daily surface reflectance data at 500 m resolution (MOD09GHK, collection 4) (Vermote et al., 2002) corresponding to the same dates and areas as the 3 Hyperion images were acquired from the EOS Data Gateway website (<http://lpdaac.usgs.gov/datapool1/datapool.asp>). The MOD09GHK product is corrected for the effects of atmospheric gases, aerosols, and cirrus clouds to provide an estimate of the surface reflectance for each band as it would be measured at ground level in the absence of atmospheric scattering or absorption. The EO-1 Hyperion sensor images the surface about 23 min prior to the corresponding Terra MODIS sensor (01:07 UTM and 01:30 UTM respectively) so, as atmosphere and sun angle conditions change little in this time, direct comparison between the two data sources is entirely valid. This product is referred as "DM" (daily MODIS).

### 4.2.3. MODIS NBAR data

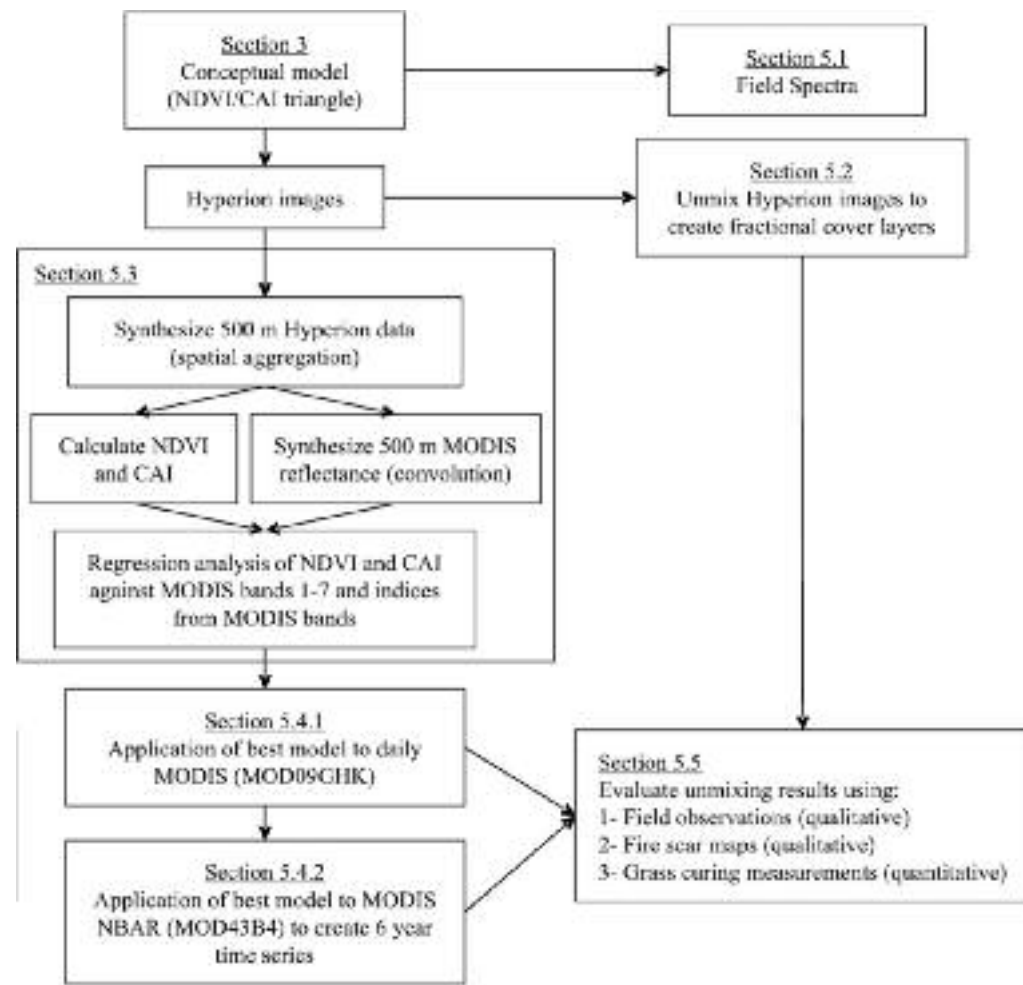
The nadir BRDF-adjusted reflectance (NBAR) product (MOD43B4) provides a 16-day, 1 km average reflectance corrected for bidirectional reflectance distribution function (BRDF) and atmospheric effects,

**TABLE 1** Wavelength ranges used for calculating the Normalized Difference Vegetation Index (NDVI) and the Cellulose Absorption Index (CAI) with field measured and EO-1 Hyperion reflectance spectra.

	Field reflectance spectra (ASD) min-max [nm] and number of channels	EO-1 Hyperion min-max [nm] and number of bands	MODIS ("synthetic MODIS", MOD09GHK and MOD43B4) band number-spectral range [nm]
$\rho_{NIR}$	676–686 (11)	681 (1)	1–520–670
$\rho_{RED}$	758–808 (11)	803 (1)	2–541–576
$\rho_{2.0}$	2007–2037 (31)	2022–2032 (2)	
$\rho_{2.1}$	2088–2118 (31)	2093–2113 (3)	
$\rho_{2.2}$	2179–2208 (30)	2184–2204 (3)	
$\rho_{2.3}$			3–459–479
$\rho_{2.4}$			4–545–565
$\rho_{2.5}$			5–1230–1250
$\rho_{2.6}$			6–1628–1652
$\rho_{2.7}$			7–2105–2155

Wavelength ranges for the MODIS bands are also shown.

FIGURE 4 A flow diagram showing the processing scheme for the analysis, time series generation and validation.



creating an apparent reflectance that is not affected by the location of the sensor relative to the pixel at the time of acquisition (Schaaf et al., 2002). This product was best suited for developing a fractional cover time series due to excellent data quality and stability. A time series of MOD43B4, collection 4 data for the Australian continent from 2000 to 2006 (Paget and King, 2008) was used to develop the fractional cover product. The time series was masked to the tropical savanna region (Fig. 1) and referred from here on as “NM” (NBAR MODIS).

## 5. Analyses

The processing scheme for the analyses is shown in Fig. 4. It shows the sequence from: (i) evaluating the conceptual model with field data and with EO-1 Hyperion data; (ii) unmixing Hyperion data to give  $f_{PV}$ ,  $f_{NPV}$  and  $f_{BS}$ ; (iii) aggregation of Hyperion to the same resolution as MODIS surface reflectance; (iv) testing of regression relationships between NDVI, CAI and MODIS surface reflectance bands; (v) application of the NDVI and selected SWIR index to unmixing of MOD43B to create a time series of  $f_{PV}$ ,  $f_{NPV}$  and  $f_{BS}$  for the 2 million km<sup>2</sup> Australian savanna region; and (vi) evaluation of fractional cover estimates with field observations, fires scars maps and grass curing measurements.

### 5.1. Field reflectance spectra

A scatterplot of CAI versus NDVI calculated for each field reflectance spectra was constructed and the relationship between the field site description and the point locations within the dataspace was assessed. The pattern was compared with the conceptual model for unmixing described in Fig. 2.

### 5.2. Hyperion unmixing

The spectral and index response were explored for each Hyperion image by carrying out three parallel processes: i) images were subjected to a Minimum Noise Fraction rotation keeping the first 20 MNF bands, followed by the pixel purity index (PPI) operation (Boardman and Kruse, 1994); ii) NDVI and CAI were calculated for each image and

the pixels located close to the vertices of the triangle were located; and iii) the spatial location of the pixels identified as pure by the PPI operation and located close to the vertices of the NDVI/CAI triangle were examined using high resolution imagery (Quickbird and Ikonos). The goal of this comparison was to confirm that the proposed NDVI/CAI unmixing yielded similar results to the more widely used pixel purity index. It was assumed that when the three Hyperion images were considered (including all phases of the dry season) there were pure pixels (30 m resolution or 900 m<sup>2</sup>) of each of the 3 endmembers included. The relative proportions of each fractional cover for any Hyperion pixel were found by solving the equations:

$$V_H = \sum f_i V_i = f_{PV} V_{PV} + f_{NPV} V_{NPV} + f_{BS} V_{BS} \quad (3)$$

$$C_H = \sum f_i C_i = f_{PV} C_{PV} + f_{NPV} C_{NPV} + f_{BS} C_{BS} \quad (4)$$

$$\sum f_i = f_{PV} + f_{NPV} + f_{BS} = 1 \quad (5)$$

where  $V_H$  and  $C_H$  are the NDVI and CAI values in a given Hyperion pixel,  $f_{PV}$ ,  $f_{NPV}$  and  $f_{BS}$  are the fractions of PV, NPV and BS in the pixel and  $V_{PV}/C_{PV}$ ,  $V_{NPV}/C_{NPV}$  and  $V_{BS}/C_{BS}$  are the NDVI/CAI values of the endmembers. It forces the values of  $f_{PV}$ ,  $f_{NPV}$  and  $f_{BS}$  to sum to unity. As a result of this condition, a pixel that falls “outside” of the triangle boundaries will have a negative or higher than 1 value in at least one endmember. When that occurred the following correction was applied:

$$C_x = 0 \text{ (if } -0.2 < C_x < 0) \quad (6)$$

$$C_x = 1 \text{ (if } -1 > C_x > 1.2) \quad (7)$$

$$C_y = C_y / (C_y + C_z) \quad (8)$$

$$C_z = C_z / (C_y + C_z) \quad (9)$$

where  $C_x$  is the value of the endmember falling “outside” the triangle and  $C_y$  and  $C_z$  are the values for the other two endmembers. If  $C_x$  was lower than -0.2 or higher than 1.2 the corresponding pixel was masked and the unmixing was not calculated. A visual inspection in the imagery showed that this occurred in some small water bodies.

### 5.3. Relationship between Hyperion unmixing and MODIS indices

It is expected that a NDVI calculated with MODIS will have a very high linear correlation with the Hyperion-derived NDVI. The biggest challenge is to find a MODIS surrogate for the CAI. Here we tested all single MODIS bands and combinations of two MODIS bands (using simple indices) with the Hyperion CAI (and also with NDVI) through simple and multiple linear regression models. Synthetic MODIS data derived from

Hyperion were used for these assessments based on the Hyperion images, spatially aggregated hyperspectral and synthetic MODIS images were developed and used to explore relationships between MODIS derived vegetation indices and those derived from Hyperion. A 500 m grid matching the location of pixels from the MOD09GHK product (daily MODIS/Terra reflectance) was overlaid on each Hyperion image. Mean reflectance at 500 m was calculated for each band at each gridcell, obtaining a simulated hyperspectral image at a resolution of 500 m. We called the 3 images obtained “H500”. We then convolved the Hyperion bands to the MODIS bands 1 to 7 (Table 1), using published spectral response functions for the MODIS Terra

sensor. We repeated this procedure with the 3 Hyperion images. The product of this process was called “SM” (Synthetic MODIS). The NDVI and CAI at 500 m were derived from the H500 images (VH500 and CH500) and synthetic MODIS bands (SMi) were obtained from the SM data. Data from the three Hyperion acquisitions were combined for the analysis. All seven MODIS bands included in the land properties products and band indices were tested for linear correlation with the CAI (Table 1) by fitting the following models:

$$SM_i = x + z \cdot C_{H500} \quad (10)$$

$$SM_j = x + z \cdot C_{H500} \quad (11)$$

where SMi is MODIS bands 1 to 7 from the synthetic MODIS and SMij are the three types of combinations of pairs of synthetic MODIS bands 1 to 7. We tested: (i) the simple difference between the i and j bands (i-j); (ii) the simple ratio between the two bands (i/j); and

(iii) the normalized difference between the two bands [(i-j)/(i+j)]. The linear correlation between MODIS bands and indices and the Hyperion NDVI (V500) was also tested:

$$SM_i = x + z \cdot V_{H500} \quad (12)$$

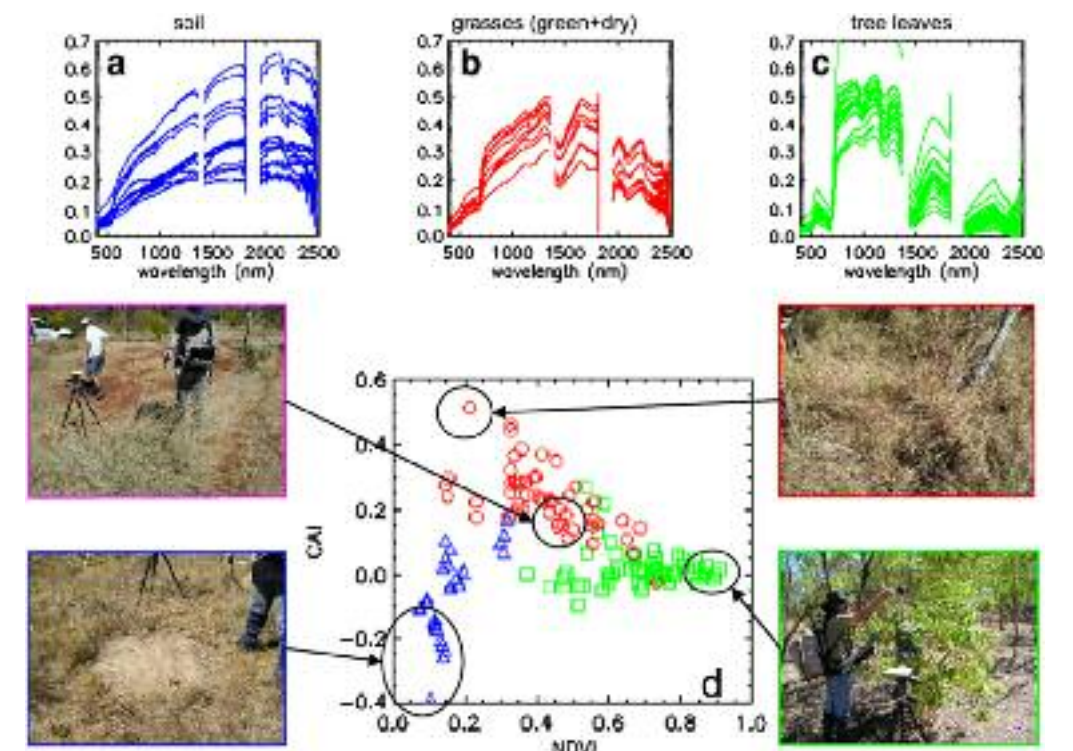
$$SM_j = x + z \cdot V_{H500} \quad (13)$$

Anticipating that no single MODIS band or two-band index will yield a satisfactory linear correlation with CAI, multiple linear correlations were also calculated between MODIS bands and the Hyperion NDVI/CAI response space, i.e. the NDVI and CAI considered simultaneously. As above, the following models were fitted:

$$SM_i = x + y \cdot V_{H500} + z \cdot C_{H500} \quad (14)$$

$$SM_j = x + y \cdot V_{H500} + z \cdot C_{H500} \quad (15)$$

FIGURE 5 Field reflectance spectra collected during July 2005 at 7 locations in the Northern Territory, Australia. The upper graphs show reflectance spectra for patches of: (a) bare soil; (b) grasses (including green and standing dead); and (c) tree leaves. The scatterplot, (d), shows the same reflectance spectra in NDVI-CAI dataspace. The pictures show examples of reflectance spectra located in different positions of the scatterplot.



#### 5.4. Application to MODIS data

##### 5.4.1. Daily MODIS (MOD09GHK)

Once the best linear model between H500 and SM was selected, the equivalent endmembers in MODIS reflectance space were located by transforming the VH500 and CH500 values into the corresponding values of SMi (individual bands) or SMij (two-band indices) using the linear models. Then a similar approach to Hyperion was implemented, and f<sub>PV</sub>, f<sub>NPV</sub> and f<sub>BS</sub> was resolved via linear unmixing.

$$V_{SM} = \sum f_i V_{SM,i} = f_{PV} V_{SM,PV} + f_{NPV} V_{SM,NPV} + f_{BS} V_{SM,BS} \quad (16)$$

$$C_{SM} = \sum f_i C_{SM,i} = f_{PV} C_{SM,PV} + f_{NPV} C_{SM,NPV} + f_{BS} C_{SM,BS} \quad (17)$$

$$\sum C_i = C_{PV} + C_{NPV} + C_{BS} = 1 \quad (18)$$

where  $V_{SM}$  is the MODIS-derived NDVI and  $C_{SM}$  is the MODIS-derived index that best matches the Hyperion-derived CAI values in a given pixel, ( $V_{SM,PV}$ ,  $C_{SM,PV}$ ), ( $V_{SM,NPV}$ ,  $C_{SM,NPV}$ ) and ( $V_{SM,BS}$ ,  $C_{SM,BS}$ ) are the values of the endmembers. The unmixing scheme was then applied to the daily MODIS data, from the MOD09GHK product corresponding to the same overpass days as the EO-1 Hyperion. The same corrections applied to the pixels falling “outside” the triangle described in Eqs. (6)–(9) were applied to the results of the linear unmixing with MODIS images. Again, a visual inspection in the images showed that the pixels masked out (those with at least one of the cover fractions  $b < 0.2$  or  $NL > 2$ ) corresponded to water bodies or clouds.

##### 5.4.2. MODIS NBAR (MOD43B4)

The unmixing process was also applied to the MODIS NBAR product (MOD43B4). This generated a series of 16-day fractional cover composites (23 per year) for the tropical savannas from 2000 to 2006.

#### 5.5. Model evaluation

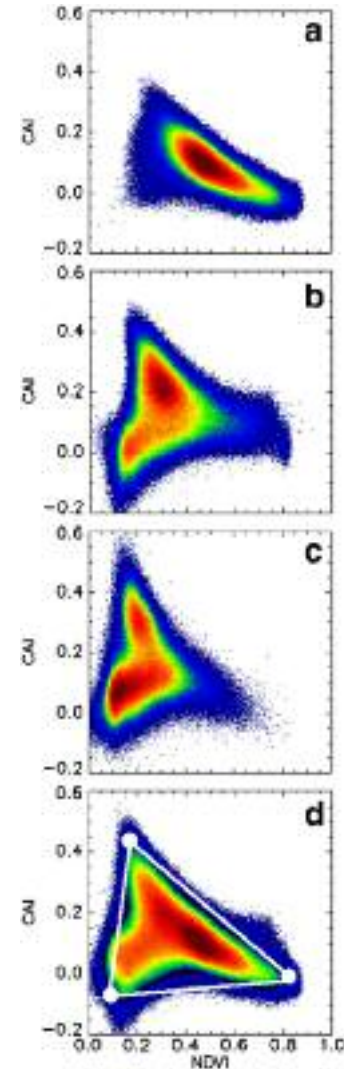
Three sources of data were used for qualitatively assessing the conceptual model and the spatial and temporal trends in fractional cover derived from Hyperion imagery and for quantitatively validating the MODIS-derived fractional cover.

##### 5.5.1. Qualitative assessment

1. Field visits took place in May and late August 2005 at 12 sites within the Hyperion transect. The visits were within 20 days of the acquisition dates for Hyperion images at the beginning of the dry season (30 April) and the end of the dry season (5 September). No in-situ quantitative measurement of vegetation fractional cover were conducted, but the general description of vegetation type and condition and the pictures taken provided a means for a qualitative evaluation of the method proposed and its sensitivity to temporal changes. The site coordinates where recorded with a standard global positioning system (GPS) receiver and later located in the Hyperion image from where the reflectance spectra were obtained using a 5×5 pixels window.

2. Fire scar data were used as a source of spatial and temporal qualitative validation for both the Hyperion-based and MODIS based fractional cover mapping. Data are produced by the North Australian Fire Information, Tropical Savannas Cooperative Research Centre. Fire scars (i.e. areas actually burned) are mapped in the Australian tropical savannas using a semi-automated algorithm with MODIS 250 m data (bands 1 and 2) as inputs. A segmentation process is applied to the difference between two consecutive 8-days MODIS composites which are then manually classified as burned or not burned by a trained analyst (<http://www.firenorth.org.au/nafi/html/help/faq.pdf>). The resultant vectorized map shows burned areas and includes the

FIGURE 6 Location of the Hyperion reflectance spectra in the space defined by the NDVI and CAI for 3 dates of 2005- (a) end of wet season (30 April); (b) middle of dry season (3 July); (c) end of dry season (5 September); and (d) the 3 dates combined. Colors indicate density of points from blue (low density) to dark red (high density). The white dots in (d) indicate the position of the fractional cover endmembers and the derived triangle. 934



date when the fire occurred. It was hypothesized that burned areas would have high amounts of non-photosynthetic vegetation prior to the fire, and high amounts of bare soil immediately after the fire. It was recognized that bush fires can burn different proportions of the fuel loads depending on fire intensity and this is not quantified by the fire scar

maps. However, the spatial and temporal coverage of these data (over the whole Australian tropical savannas) was an invaluable source of qualitative evaluation of the method developed here.

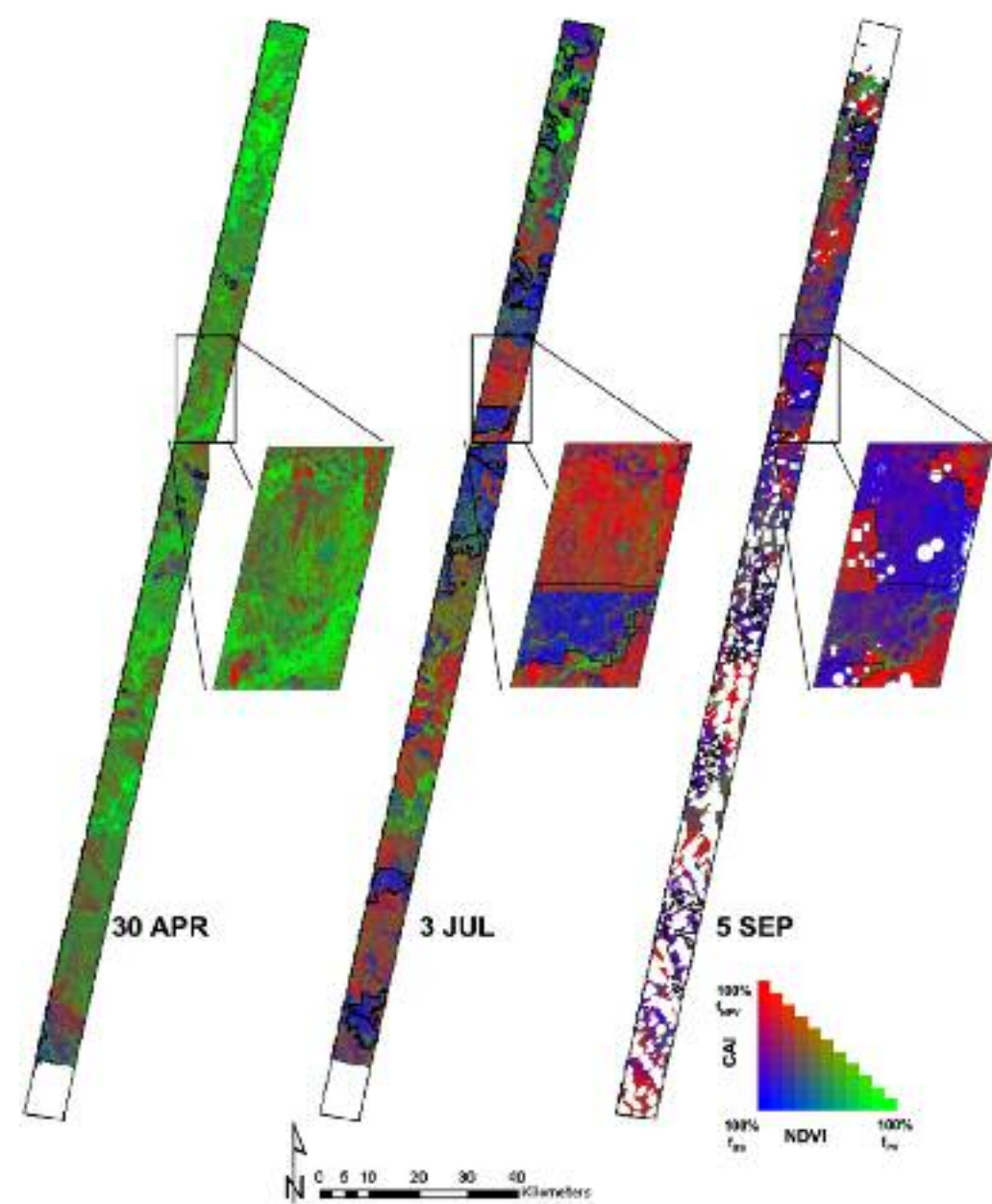
##### 5.5.2. Quantitative validation

Grass curing data provided a quantitative validation of the fractional cover mapping performed with the MODIS NBAR data. Grass curing refers to the percentage of dead

vegetation and was measured with the “Levy rod” method. A modified point intercept method, based on the point quadrat method developed by Levy and Madden (1933), involving a single thin metal rod (Anderson et al., 2005) was used to assess the percentage dead and green vegetation at each sample site. The rod was driven into the ground at 1 m intervals along two perpendicular 20 m transects. Vegetation touching the rod

was counted and visually classified as dead or live. The total number of touches along each transect were then tallied and converted to percentage cured. Samples were collected in ten locations in 2005 and 2006 every two weeks throughout the dry season until the grasses were either completely cured or the wet season commenced. Six sites were located in the tropical savannas. Another four sites were located in the west and southeast of Australia.

FIGURE 7 Result of the vegetation fractional cover unmixing based on the NDVI and CAI for the three Hyperion images of 2005- end of wet season (30 April), middle of dry season (3 July) and end of wet season (5 September). The proportions of fractional cover are shown in RGB as indicated in the color legend. White areas in the September image are caused by manual cloud masking. Black lines in each map indicate fires occurred during the previous 30 days of each image, obtained from fire scars maps generated from MODIS 250m images. The location of the Hyperion imagery in Northern Australia is provided on Fig. 3.



Although not tropical savannas, those four sites also have open grassy vegetation and are included. Fractional cover values estimated for the 1 km pixel were extracted at the corresponding locations. Since the curing measurements only included proportions of dry and green biomass to total biomass (without considering bare soil), the estimated fractional cover was recalculated by combining  $f_{PV}$  and  $f_{NPV}$  into the fractions of total vegetation. Curing observations of dry biomass were compared with the values obtained from dividing  $f_{NPV}$  by the sum of  $f_{NPV}$  and  $f_{PV}$ , and observations of green biomass were compared with the values obtained from dividing  $f_{PV}$  by the sum of  $f_{NPV}$  and  $f_{PV}$ .

## 6. Results

### 6.1. Field reflectance spectra

Measurements of bare soil, tree leaves and grasses formed a triangle when plotted in a NDVI/CAI scatterplot (Fig. 5). Tree leaves occupied the “right” portion of the triangle, with high NDVI and intermediate or low CAI values. Grasses (including green, dry and standing dead biomass) dominated in the “top left” portion of the triangle (low NDVI and high CAI) but in some cases also occurred towards the “right” side. Bare soil reflectance spectra occupied the “lower left” part of the triangle, with both low NDVI and CAI values. Photos from each spectral measurement site showed that grass reflectance spectra dominated by dry biomass tended to have the highest CAI and lowest NDVI values and that grass reflectance spectra from more “open” sites (i.e. low basal cover and high bare soil) formed the central portion of the data triangle.

TABLE 2 Model parameters (x and y) and Pearson correlation coefficients (r) from the linear models fitted between MODIS individual bands and indices calculated with 2 MODIS bands and Hyperion-derived NDVI (a) and CAI (b).

NDVI					CAI						
Model	a	b	x	y	r	Model	a	b	x	y	r
M4	NIR	RED	0.129	0.039	0.993	M2	SWIR2	BLUE	0.165	0.396	0.737
M3	RED	NIR	0.695	-0.805	-0.978	M2	SWIR2	GREEN	0.127	0.378	0.734
M3	NIR	RED	0.260	0.629	0.941	M3	SWIR1	NIR	0.028	0.233	0.731
M3	NIR	GREEN	1.516	-4.543	0.940	M1	SWIR2	-	0.191	0.427	0.689
M3	SWIR1	SWIR2	0.694	1.220	0.935	M2	SWIR2	RED	0.124	0.270	0.664
M4	SWIR2	SWIR1	0.131	-0.517	-0.933	M2	SWIR3	SWIR2	0.089	-0.255	-0.625
M4	SWIR1	RED	0.300	0.615	0.929	M2	RED	BLUE	0.041	0.106	0.622
M3	SWIR1	RED	1.049	8.451	0.929	M2	RED	GREEN	0.094	0.088	0.614
M4	SWIR3	NIR	0.235	-1.198	-0.927	M3	RED	GREEN	1.052	1.183	0.606
M3	SWIR2	SWIR1	1.237	-0.018	-0.919	M3	SWIR1	NIR	1.153	0.806	0.597

Four types of linear models were fitted:  $M_1 = x + yV_{H500} + zC_{H500}$  and  $M_2 = x + yC_{H500}$

where  $V_{H500}$  and  $C_{H500}$  are the NDVI and CAI derived from the spatially aggregated Hyperion (H500),  $M_i$  is the dependant variable and has four configurations:  $M_1$ : a single MODIS band ( $a = 1, 7$ );  $M_2$ : difference between two MODIS bands ( $a = b$ );  $M_3$ : simple ratio between two MODIS bands ( $a/b$ ); and  $M_4$ : normalized difference between two MODIS bands  $[(a - b)/(a + b)]$ . In all cases we used data from the three Hyperion bands resampled to 500 m (H500), taken simultaneously ( $n = 15,188$ ). The best 10 models sorted by descending order of  $r$  are reported. The model selected as surrogate for  $C_{H500}$  is highlighted in gray.

6.2. Hyperion unmixing  
Reflectance spectra obtained from the three Hyperion images formed a triangular shape when plotted in a NDVI/CAI scatterplot (Fig. 6), corresponding to the conceptual model (Fig. 2). There was a trend of decreasing NDVI and an increase in the range of CAI as the dry season advanced, coincident with vegetation drying and the occurrence of fires in the area. When the three dates were considered simultaneously the NDVI ranged between 0 and 0.8 and the CAI ranged between -0.1 and 0.4 (Fig. 6d). Ideally, field measurements of vegetation

fractional cover in large areas with homogeneous fPV, fNPV and fBS cover are needed to locate endmembers in the NDVI/CAI space. Since such data were lacking, locations were derived by visually examining the land cover properties of Hyperion pixels located near the vertices of the triangle within very high resolution imagery. Visual examination using the Google Earth software (which coincidentally included Quickbird images acquired on 15 May 2005 and 13 August 2005 in the area, i.e. within 15 and 23 days of the first and third Hyperion images

respectively) suggested that potential endmembers were mostly covered with a single vegetation type. Endmember locations (the triangle vertices) were defined as follows (Fig. 6):

$$f_{PV}: V_H = 0.8, C_H = 0$$

$$f_{NPV}: V_H = 0.175, C_H = 0.4$$

$$f_{BS}: V_H = 0.1, C_H = -0.1$$

Vegetation fractional cover obtained from linearly unmixing NDVI and CAI to  $f_{PV}$ ,  $f_{NPV}$  and  $f_{BS}$  are shown in Fig. 7. The 30 April image was dominated by photosynthetic vegetation (majority of green pixels). On July 3 (mid of the dry season) there was more heterogeneity in fractional cover, with all three covers dominating small areas. At the end of the dry season (5 September) the Hyperion scene is dominated by large patches of  $f_{NPV}$  and  $f_{BS}$ .

### 6.3. Relationship between Hyperion unmixing and MODIS indices

There was a highly significant ( $p < 0.001$ ) positive linear correlation ( $r = 0.993$ ) between a MODIS-derived NDVI and the NDVI calculated from Hyperion bands (Table 2a). Several other 2-band indices constructed with MODIS also showed high (positive or negative) correlations with Hyperion-derived NDVI, including combinations of the NIR and visible bands, and the SWIR1 and SWIR2 bands. Correlations between single

MODIS bands or combinations of 2 MODIS bands and the Hyperion-derived CAI were lower ( $r \leq 0.75$ ) (Table 2b). The best model out of all tested was between the CAI and the difference between MODIS bands 6 and 3 (SWIR2 and BLUE) with  $r = 0.737$ . Several MODIS models had high ( $r \geq 0.9$ ) multiple correlation coefficients with the NDVI/CAI space in the multiple regression analysis. The three best models (measured through the correlation coefficient,  $r$ ) included the MODIS NDVI and the simple ratio between the NIR and the red or green bands (Table 3). These models, however, were highly sensitive to the Hyperion NDVI and relatively insensitive to the Hyperion CAI, as shown through the ratio of the y and z parameters. In other words, those models fitted (linearly) very well to the plane defined by NDVI and CAI, but changed mostly as a function of NDVI rather than CAI and, consequently, are not useful for discriminating between fNPV and fBS. Two models showed both a high  $r$  and a good sensitivity to the CAI (as shown by the ratio  $z/y$ ): the ratio of SMSWIR3 to SMSWIR2 (SMSWIR3/SWIR2, where SMSWIR3 and SMSWIR2 are MODIS bands 7 and 6 respectively) and the normalized difference index between those two bands

$[(SM_{SWIR3} - SM_{SWIR2}) / (SM_{SWIR3} + SM_{SWIR2})]$  (Table 3 and Fig. 8). In both cases, the multiple correlation coefficients were around 0.95 and the y and z parameters were very similar, meaning that the two MODIS-derived indices are sensitive to NDVI and CAI simultaneously. These results indicate that the spectral information sampled by the three MODIS SWIR bands is sensitive to the fractional cover of vegetation mapped by the Hyperion-derived NDVI and CAI. When

both NDVI and CAI are low (the bare soil "corner" in the triangle scheme), the ratio of  $SM_{SWIR3}$  to  $SM_{SWIR2}$  is close to 1, indicating a relatively flat reflectance spectra in those two bands (Fig. 8). When the NDVI or the CAI increases (more vegetation, either green or dry) the ratio of  $SM_{SWIR3}$  to  $SM_{SWIR2}$  decreases. The simple ratio of  $SM_{SWIR3}$  and  $SM_{SWIR2}$  (hereafter referred to as  $SM_{SWIR3}/SM_{SWIR2}$ ) was selected because of its high correlation with the NDVI/CAI space and its relative high sensitivity to  $C_{H500}$  (Table 3).

When this index was combined with the  $V_{H500}$  a triangular pattern was evident (Fig. 8). While the response space is flattened and rotated relative to the conceptual model and the NDVI-CAI space from Hyperion and the two indices are not orthogonal (as  $V_{H500}$  and  $C_{H500}$ ); they still form a dataspace within which vegetation fractional cover can be unmixed.

FIGURE 8 Three dimensional scatterplot showing the relationship between the spatially aggregated Hyperion-derived NDVI (VH500), CAI (CH500) and the Synthetic MODIS ratio of SWIR3 and SWIR2 (MODIS bands 7 and 6 respectively). The plane shown as a meshed surface corresponds to the multiple linear model (shaded in Table 3). The three 2D scatterplots in the right show the projection of the data into the three sides of the cube. The green, red and blue circles show the location of the fPV, fNPV and fBS endmembers respectively in each projection.

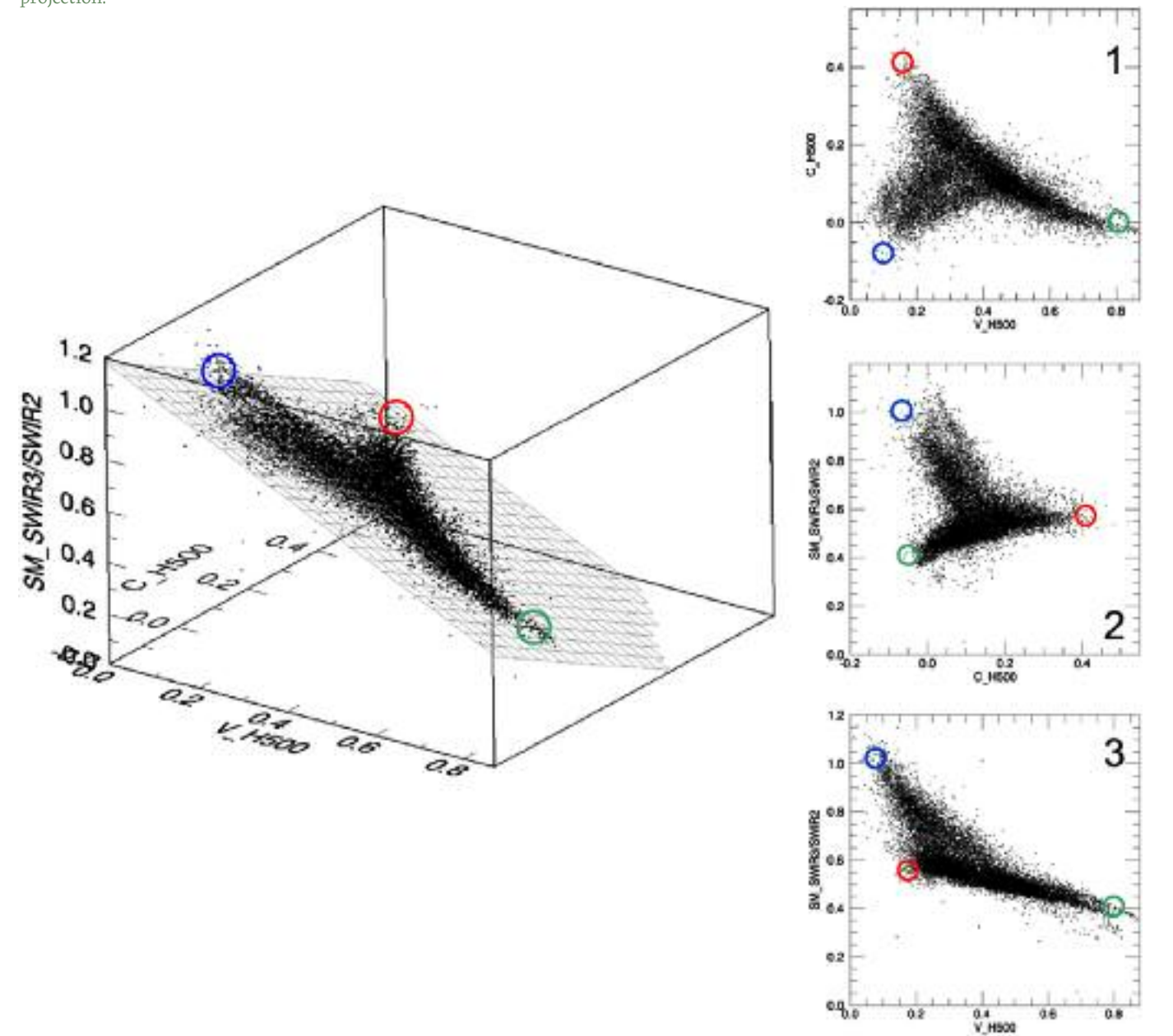


TABLE 3 Results from the multiple linear regression models fitted between MODIS individual bands and indices calculated with 2 MODIS bands and Hyperion-derived NDVI and CAI ( $V_{H500}$ ,  $C_{H500}$ ).

Model	a	b	x	y	z	r	z/y
M4	NIR	RED	-0.101	0.857	0.149	0.997	0.172
M3	RED	NIR	0.741	-0.848	-0.229	0.988	0.279
M3	NIR	GREEN	1.172	-4.889	1.823	0.960	0.373
M4	SWIR1	RED	-0.242	0.674	0.311	0.959	0.462
M4	SWIR3	SWIR1	-0.169	-1.089	-0.679	0.955	0.624
M1	RED	SWIR1	0.571	-0.590	-0.722	0.951	0.546
M4	SWIR3	SWIR2	-0.040	-0.640	-0.576	0.952	0.900
M3	SWIR1	SWIR2	1.006	-0.851	-0.844	0.948	0.962
M4	NIR	GREEN	-0.247	0.595	0.349	0.945	0.585
M4	SWIR3	NIR	-0.322	-1.285	-0.452	0.944	0.359

The structure of the models fitted was:  $M_i = x + yV_{H500} + zC_{H500}$

where  $V_{H500}$  and  $C_{H500}$  are the NDVI and CAI derived from the spatially aggregated Hyperion (H500).  $M_i$  is the dependant variable and has four configurations:  $M_1$ : a single MODIS band ( $a = 1, 7$ );  $M_2$ : difference between two MODIS bands ( $a = b$ );  $M_3$ : simple ratio between two MODIS bands ( $a/b$ ); and  $M_4$ : normalized difference between two MODIS bands  $[(a - b)/(a + b)]$ . The model parameters x, y and z, the multiple correlation coefficient (r) and the ratio of z to y for the best 10 models sorted by r in descending order are reported. Data from the three Hyperion bands resampled to 500m, taken simultaneously ( $n = 15,188$ ) were used. The model selected as surrogate for  $C_{H500}$  is highlighted in gray.

#### 6.4. Application to MODIS data

##### 6.4.1. Daily MODIS (MOD09GHK)

The combination of the MODIS indices  $SM_{SWIR3/SWIR2}$  and  $SM_{NDVI}$  proposed above was applied to daily MODIS data obtained from the MOD09GHK product. First the Hyperion NDVI ( $V_{H500}$ ) was converted to equivalent values of MODIS NDVI ( $V_{DM}$ ) using the linear

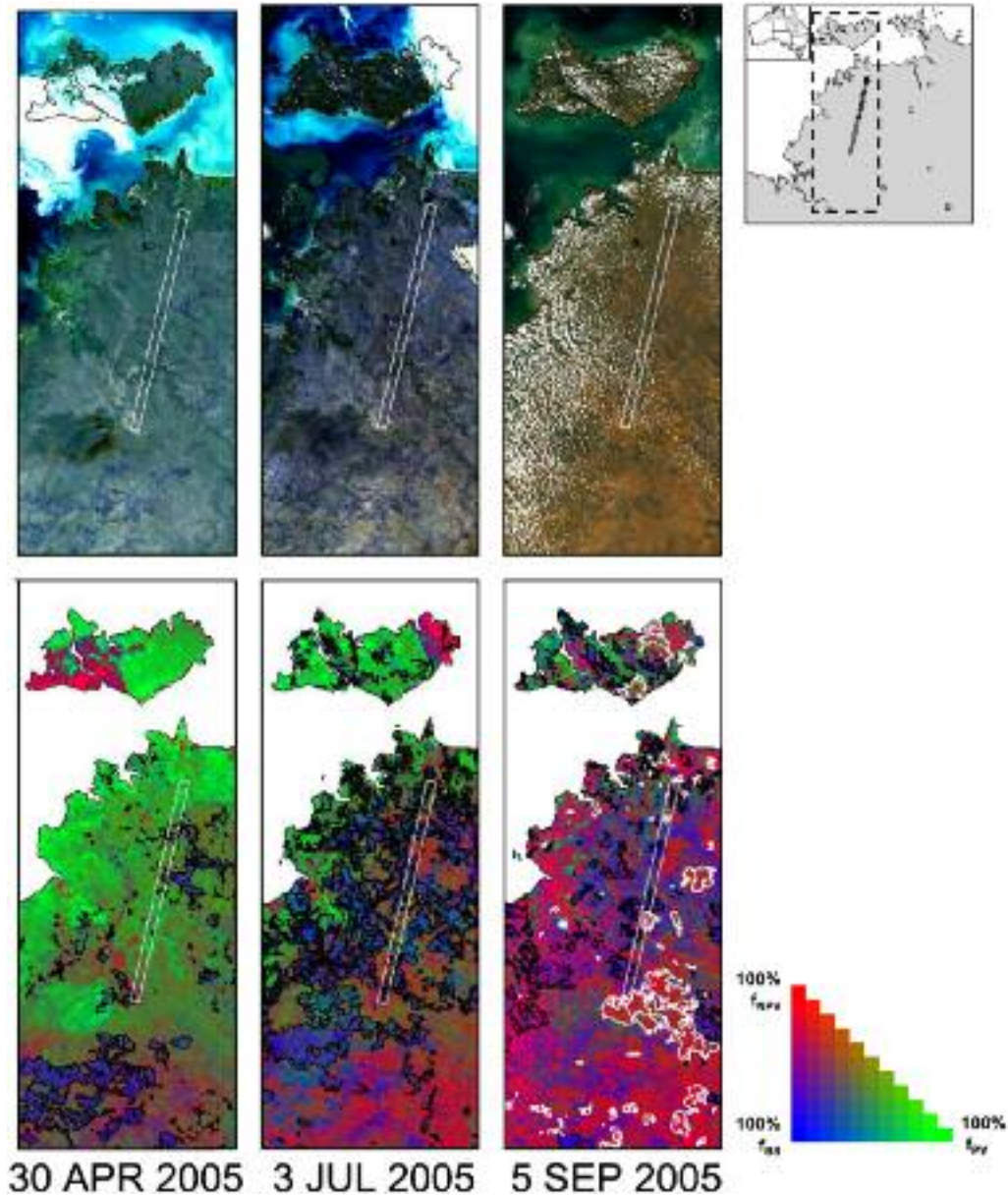
model in Table 2a. Then NDVI/CAI values corresponding to the three endmember obtained with Hyperion imagery were converted to MODIS values of  $SM_{SWIR3/SWIR2}$  through the multiple regression model shaded in Table 3. The locations of the endmembers in the  $SM_{NDVI}$  and  $SM_{SWIR3/SWIR2}$  space were

$$f_{fPV}: SM_{NDVI} = 0.814, SM_{SWIR3/SWIR2} = 0.318;$$

$$f_{fNPV}: SM_{NDVI} = 0.297, SM_{SWIR3/SWIR2} = 0.490; \text{ and}$$

$$f_{fBS}: SM_{NDVI} = 0.170, SM_{SWIR3/SWIR2} = 1.02$$

FIGURE 9 Spatial distribution of the vegetation fractional cover estimation using daily MODIS data in a site in Northern Australia. The 3 maps above show true color (MODIS bands 3,4,1) and help identifying clouds. The maps below show the result of the unmixing method using the SWIR3/SWIR2 ratio and NDVI. The proportions of fractional cover are shown in RGB as indicated in the color legend. The white rectangles in the maps indicate the location of the Hyperion images. In the maps below, black polygons indicate areas burnt during the 45 days before the image acquisition and white polygons (only present in the September image) indicate areas burnt after September 5th or not burnt in 2005. Burnt areas (fire scars) were mapped by the Tropical Savannas CRC (see text).

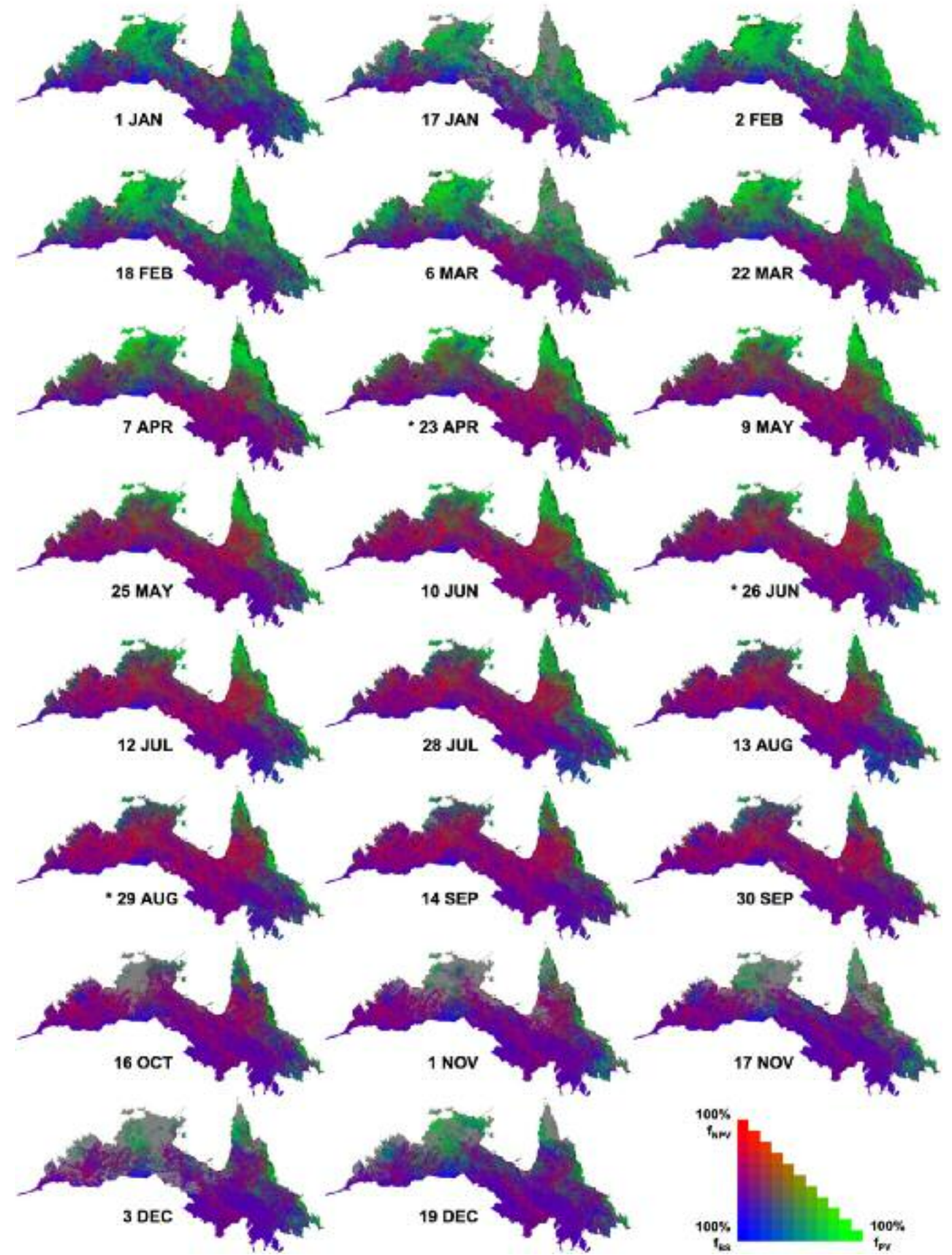


The result of applying the unmixing to daily MODIS images is shown in Fig. 9. As observed when the fractional vegetation cover was resolved with Hyperion (Fig. 7), the April image (end of the wet season) is dominated by photosynthetic vegetation. In July (mid of the dry season) the area is mixed with patches of  $f_{fPV}$ ,  $f_{fNPV}$  and  $f_{fBS}$  and in September (end of dry season), the area is dominated by mixtures of  $f_{fNPV}$  and  $f_{fBS}$ . It can also be seen that presence of clouds in the September image results in the algorithm producing spurious results (high  $f_{fNPV}$ ).

##### 6.4.2. MODIS NBAR (MOD43B4)

The selected index model and unmixing schemes was applied to 16-day MODIS NBAR composites from 18 February 2000 to 31 December 2006. The results for the 23 composites of 2005 are shown in Fig. 10. There is a general temporal pattern determined by the monsoonal precipitation. Vegetation dries during the dry season (April to October) and it is also when fire activity is concentrated, which is reflected in the fractional cover with high  $f_{fNPV}$  and the spread of patches of  $f_{fBS}$ . The monsoonal rains occurring from October to March generate the flush of vegetation growth. It is also evident, particularly in the Northern part of the tropical savannas, that the compositing scheme applied to the NBAR product does not completely overcome

FIGURE 10 Spatial distribution of  $f_{fPV}$ ,  $f_{fNPV}$  and  $f_{fBS}$  for the Australian tropical savanna zone in 2005. The proportions of fractional cover are shown in RGB as indicated in the color legend. The date below each map is the first day of the 16-day composite. Gray pixels indicate masked areas in the NBAR product, due to the unsuccessful cloud removal in the compositing algorithm. Black pixels indicate areas where the unmixing method failed (see text for details).



the contamination of clouds during the wet season (pixels masked likely due to clouds shown in gray).

The temporal pattern of  $f_{PV}$ ,  $f_{NPV}$  and  $f_{BS}$  was extracted for the major grassland cover types shown in Fig.1c split into major species types after Hill et al.

(2005) (Fig. 11). These grassland cover types are strongly correlated with the rainfall and soil type with the annual tallgrass (Shizachyrium and Sorghum spp) occupying the wetter savanna (Fig. 11a), the perennial tallgrass occupying somewhat dryer savanna

(Sehima and Heteropogon spp, Fig. 11b), the perennial shortgrass occupying grasslands (Dicanthium spp) and more seasonally variable savanna (Aristida/Bothriochloa spp) (Fig. 11c), the perennial tussock grassland occupying the heavy soils with little tree cover

(Astrebla spp) (Fig.11d), and the perennial hummock grassland and woodland (Triodia spp) occurring at the boundary between the savanna and the arid zone (Fig.11e). The main ecologically-driven differences in the signatures are-

a) a difference in baseline  $f_{PV}$  between more wooded types and the grassland types;

b) a greater amplitude of  $f_{PV}$  and  $f_{NPV}$  signal in the monsoonal annual tallgrass woodlands diminishing in the perennial tallgrass woodlands and lowest for the grasslands; and

c) a higher fraction cover of  $f_{BS}$  in the grasslands and hummock grass woodlands than in the annual and perennial tallgrass woodlands. These properties and the seasonal and interannual variations characterise the systems, and local variations due to over-grazing and severe fires are detectable and therefore become a significant input to models of carbon and water performed in this region.

### 6.5. Model evaluation

6.5.1. Qualitative assessment  
Assessment of the Hyperion unmixing using fire scar data showed a very good agreement with the expected patterns of fractional cover (Fig. 7) so, as expected, areas burnt in the 30 days prior to the image acquisition had high proportions of  $f_{BS}$ . It is also evident, particularly in the July and September images, the high amount of  $f_{NPV}$  of areas that were burnt immediately after the date when the image was acquired. The unmixed fractional cover performed with daily MODIS data were also qualitatively assessed against the fire scar data generated by the Tropical Savannas CRC (Fig. 9). As in the Hyperion case, areas recently burned were unmixed with high proportion of bare soil and areas not burned remained with high proportions of non-photosynthetic vegetation. A further qualitative assessment of Hyperion

unmixing of vegetation fractional cover using the photography acquired at 12 sites in May and late August 2005 showed good correspondence (Fig. 12). Some sites show a very contrasting pattern in fractional cover between the beginning and the end of the growing

season. For example, the site Daly River 1 had 61%  $f_{PV}$  in April but was burnt in September and consequently had 68% of  $f_{BS}$  and 34% of  $f_{NPV}$ . The other sites with trees and shrubs that did not burn (Daly River 2, Small Shrub Woodlands and Mimosa Patch 1 and 2) had a less drastic

temporal change and maintained  $f_{PV}$  of ~15-30% at the end of the dry season. The grassland sites had contrasting temporal changes according to the visually estimated cover. The site Spear Grass Plain changed from 85% to 8%  $f_{PV}$  with  $f_{NPV}$  increasing from 7% to 79% between April

and September. In contrast, the site Grassy Plain decreased from 17%  $f_{PV}$  in April to 0%  $f_{PV}$  in September. Finally, the Mango Plantation did not show much change in fractional cover, coincident with the qualitative assessment from the photos.

FIGURE 11 Time traces of fractional cover for major under-storey grassland types within the tropical savanna zone contrasted with rainforest. The under-storey grassland constitutes five main growth forms- a) annual tall grass (Shizachyrium spp. and Sorghum spp. woodland); b) perennial tall grass (Sehima/Chrysopogon spp. and Heteropogon spp. woodland); c) perennial short grassland (Dicanthium spp. grassland and Aristida/Bothriochloa woodland); d) perennial tussock grassland (Astrebla spp. – Mitchell – grassland); and e) perennial hummock grassland (Triodia spp. grassland and woodland). The maps show the location of the grassland types.

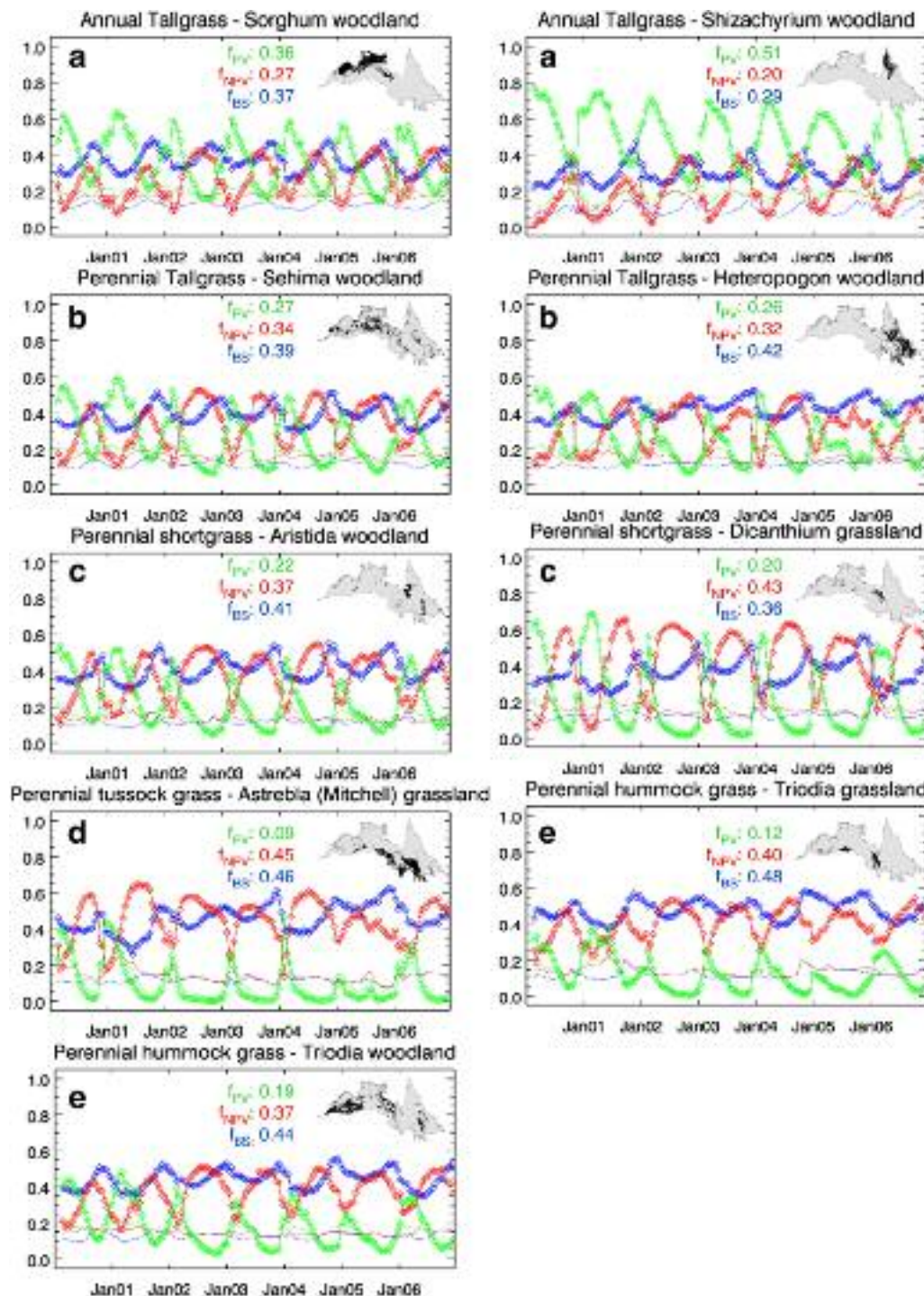


FIGURE 12 Qualitative validation of the fractional cover estimated with Hyperion imagery. Each set of pictures and graphs corresponds to one of 12 sites visited from 16 to 19 of May and 29 to 31 of August 2005. The left graphs show the reflectance spectra derived from Hyperion images for the April (green curve), July (black curve) and September (blue curve) images from 400 to 2400 nm. The right graphs show the position of each spectrum in the NDVI (x-axis) and CAI (y-axis) space from April to September (red dots and line) and the position of the endmembers (black lines). The derived  $f_{PV}$ ,  $f_{NPV}$  and  $f_{BS}$  are shown in each picture.

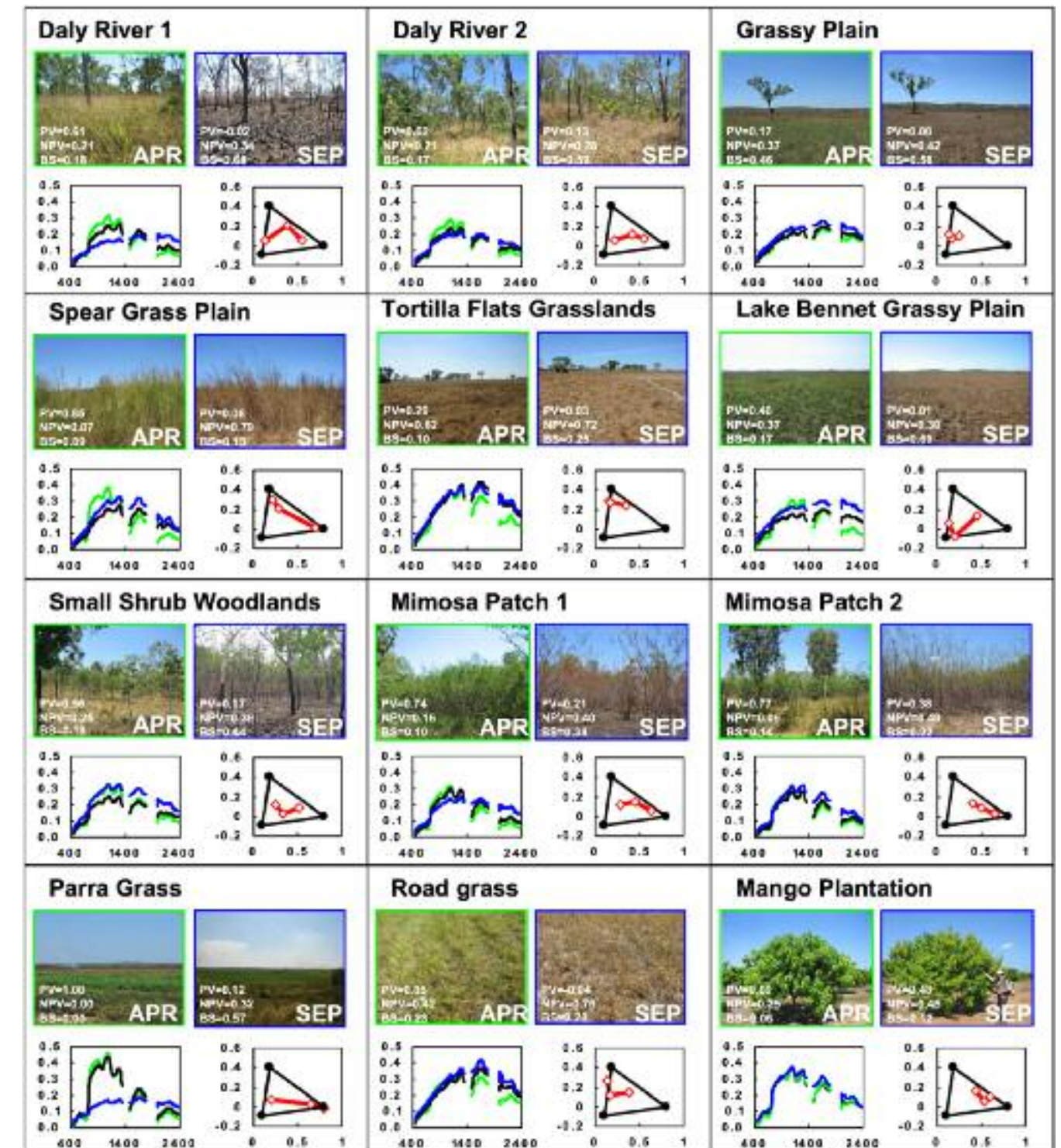
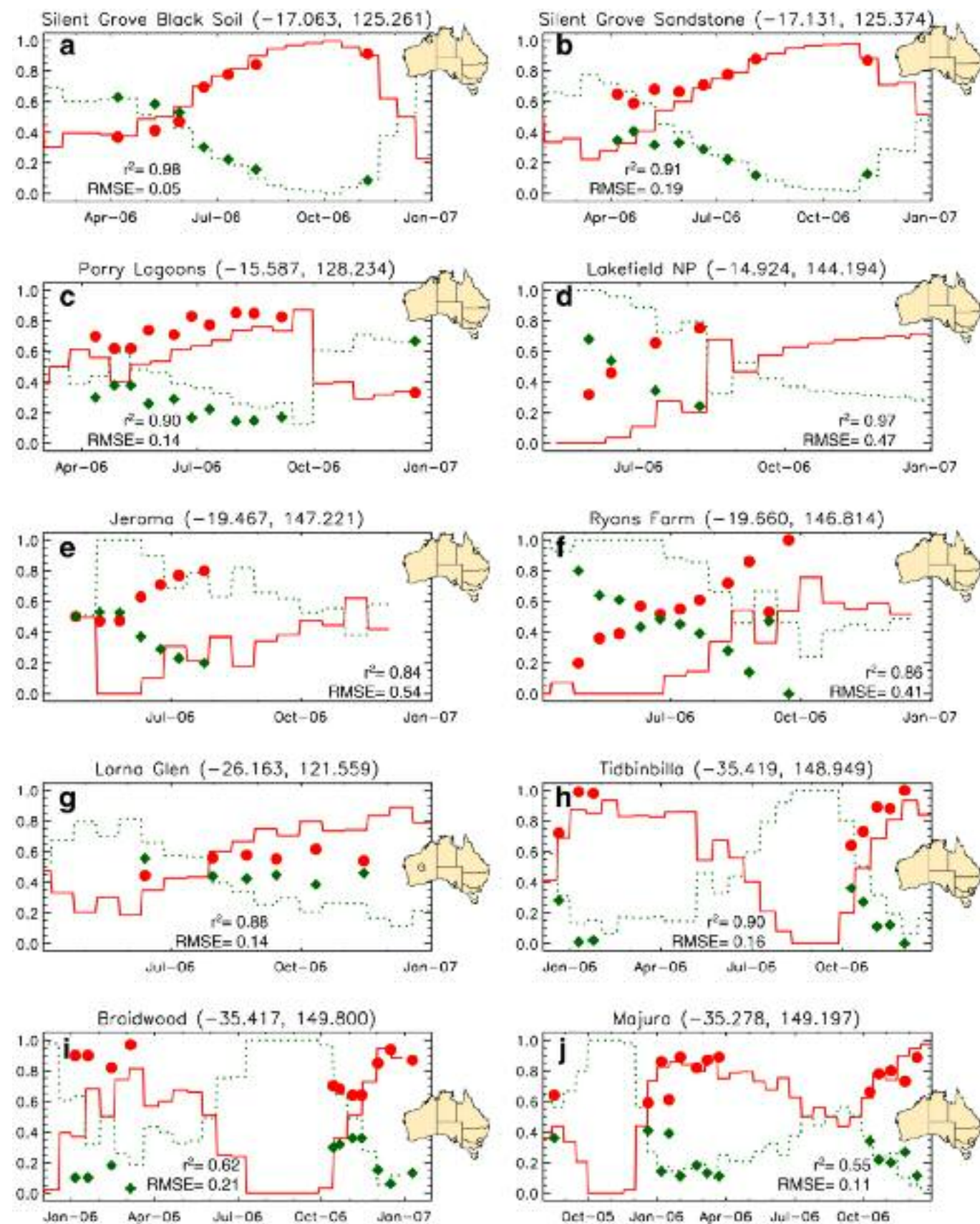


FIGURE 13 Comparison between estimated and observed fPV and fNPV in ten sites across the Australian continent. All sites included grassy vegetation and (a) to (f) were located in the tropical savannas. The lines show the estimations from MODIS NBAR and the symbols represent the curing field measurements. Red solid lines and circles indicate nonphotosynthetic vegetation and green-dotted lines and diamonds indicate photosynthetic vegetation. The remote sensing estimates of fPV and fNPV were recalculated as proportions of total vegetation cover (i.e.  $f_{PV} + f_{NPV} = 1$ , see text for details). The coefficient of determination ( $r^2$ ) and root mean square error (RMSE) between observed and predicted fPV and fNPV are shown. The numbers in brackets after the site name are the latitude and longitude in decimal degrees.



6.5.2. Quantitative validation  
 Grassland curing data from ten sites provided the objective basis for validation of the fractional cover product (allowing for the lack of soil fraction data). There was a strong correlation between  $f_{PV}$  and  $f_{NPV}$  estimated with MODIS NBAR and the grass curing estimates (Fig.13). For two sites in the Kimberlies with contrasting soil type (Silent Grove black soil and sandstone) there was very little bias between predicted and observed and high temporal correlation. In 3 sites in northwest Queensland, (Lakefield (Fig. 13d), Jeroma (Fig. 13e) and Ryans Farm (Fig. 13f)) the remote sensing method underestimated the fNPV proportions by 45%, 54% and 39% respectively. However, these grass curing sites were situated in very heterogeneous land cover and this resulted in a high level of mixed cover in the MODIS 1 km resolution. Additionally, it is possible that nonlinear mixing due to multiple scattering produced an overestimation of the fPV proportions at these sites (Huete, 1988; Ray and Murray, 1996; Roberts et al., 1993). Nevertheless, the remote sensing estimates still captured the seasonal changes in  $f_{PV}$  and  $f_{NPV}$  as reflected in the high  $r^2$  values. At the Parry Lagoons site, the proportions of fNPV were underestimated by approximately 14% during 2006, but the model successfully detected the sudden drop in  $f_{NPV}$  caused by a fire in Sep 2006. In the three sites in the southeast of Australia (Tidbinbilla (Fig. 13h), Braidwood (Fig. 13i) and Majura (Fig. 13j)) the unmixing method also showed a good agreement (RMSE between 0.11 and 0.21) with the  $f_{PV}$  and  $f_{NPV}$  measured and, as in the previous cases, captured the seasonal cycle of vegetation greening-drying.

## 7. Discussion

The results obtained from reflectance spectra derived from both field measurements

and Hyperion imagery support the hypothesis that  $f_{PV}$ ,  $f_{NPV}$  and  $f_{BS}$  can be resolved within the NDVI and CAI dataspace. While the NDVI separated green vegetation from dry vegetation and soil, the CAI discriminated between the soil and dry vegetation. Daughtry (2001) and Daughtry et al. (2005) found a similar pattern in agricultural paddocks, where NDVI and CAI separated green soil, and Marsett et al. (2006) found that the SATVI, based on a combination of the red and the SWIR bands from LANDSAT ETM and the soil line concept, could be used to distinguish green, and senescent vegetation from soil in arid grasslands. Daughtry et al. (2006) used those patterns for mapping tillage practices using a non-parametric thematic classification system. Here one step further is taken using a continuous classification scheme, where each reflectance spectra (or hyperspectral pixel) is assigned a proportion of the three endmembers according to its particular combination of NDVI and CAI.

Most of the previous research (e.g., Asner and Lobell, 2000; Lobell et al., 2001) aimed at mapping fractional cover with image spectroscopy focused on the use of spectral mixture analysis from the original spectral bands in the SWIR and NIR regions. That approach proved to be very satisfactory when the AVIRIS sensor was used. The few studies that applied the same method with Hyperion images showed a more limited success (Asner and Heidebrecht, 2003; Miura et al., 2003), due to the lower signal-to-noise ratio of the Hyperion sensor. In this current analysis quantitative positioning of the endmembers was derived by locating the most extreme pixels from the Hyperion imagery. By having mapped a large area in three contrasting stages of the growing season by a sensor

with 30 m pixels, there are at least a few (tens to hundreds) pure pixels of each fractional cover type included in the data. Applying this assumption the NDVI/CAI values for "pure"  $f_{PV}$ ,  $f_{NPV}$  and  $f_{BS}$  pixels were located and their fractions unmixed.

One important assumption in our method is that the mixing of fractional cover in NDVI and CAI is linear. This assumption is partly supported by previous studies. First, Lu et al. (2003) showed a linear relationship between NDVI and field percent cover (FPC), and between the NIR-RED simple ratio (SR) and LAI in Australian vegetation and suggested that the saturation of both NDVI and FPC could explain this linear pattern. Second, Nagler et al. (2003) found a linear relationship between CAI and percent residue cover of crops and trees. Therefore, a linear unmixing of fractional cover in NDVI/CAI is plausible when the fractional cover refers to exposed field percent cover.

No single MODIS band or combination of two MODIS bands was able to provide the same information as the CAI derived from hyperspectral imagery. The MODIS surface reflectance and NBAR products are not sensitive to the absorption features between 2000-2200 nm. However, within the field reflectance spectra acquired here, soils had similar reflectance at 1600 and 2200nm. This provided a strong contrast to both green and dry vegetation which showed a much lower reflectance at 2200 nm than at 1600 or 1200 nm. Therefore, an index that captured this difference in spectral response would be useful for separating soils from green or dry vegetation. Although the simple ratio of SWIR3 to SWIR2 was chosen, the normalized difference index between these two bands would have yielded a similar result (Table 3). The MODIS SWIR3/SWIR2 index did not

show a high linear correlation with CAI because it was also correlated with the NDVI (Table 2b and Fig. 8). When the CAI is high (i.e. high  $f_{NPV}$ ) the SWIR3/SWIR2 ratio will be low. But at low values of CAI, the SWIR3/SWIR2 ratio will be either high (bare soils, low NDVI) or low (green vegetation, high NDVI).

One key aspect to consider in the application of these spectral properties is the validity of the "flat SWIR reflectance spectra" in different soil types and moisture contents. Several studies have shown that the main effect of increased moisture on soil reflectance is a reduction in albedo. Drier soils had higher reflectance in all bands, but the "shape" of the reflectance spectra does not change significantly (Galvao et al., 2001; Lobell and Asner, 2002; Nagler et al., 2000; Palacios-Orueta and Ustin, 1998). Lobell and Asner (2002) showed that the four soil types analyzed had a SWIR3/SWIR2 ratio (MODIS bands 7 and 6) that ranged between 0.8 and 1.1. In soil reflectance spectra from sites in North America, South America and Hawaii the main variability was in albedo, and the "shape" of reflectance spectra in the SWIR did not change greatly (Asner et al., 2005a; Asner and Heidebrecht, 2003). Similarly, it was shown in ten soil types from France that the main effect of wetting was decreasing reflectance, but importantly the ratio of reflectance at 2200 nm and 1670 nm did not change (Weidong et al., 2002, see Fig. 4 therein). These results are consistent with the values reported here, wherein pixels with high proportions of bare soil (upper left part of the plane in Fig. 8) had a SWIR3/SWIR2 ratio between 0.9 and 1.1. While a more quantitative analysis using soil and litter reflectance spectra is desirable, particularly in the Australian context, the assumption of soils having a low spectral variability in the SWIR appears reasonable.

## 8. Conclusions

In this paper, a simple, robust method for quantitatively mapping  $f_{PV}$ ,  $f_{NPV}$  and  $f_{BS}$  across the Australian tropical savanna region was developed. The theoretical basis for the method relies in combining the spectral feature of green leaves in the red-near infrared and the spectral feature observed in non-photosynthetic vegetation at 2000–2200 nm and builds upon Daughtry et al. (2005, 2006) in cropping systems, and Marsett et al. (2006) in arid grasslands. Our approach used Hyperion hyperspectral data to establish a method using the NDVI and the CAI. Then regression analysis was used to find a surrogate index for the CAI in MODIS surface reflectance data. The selected SWIR index along with calculated NDVI were used to unmix  $f_{PV}$ ,  $f_{NPV}$  and  $f_{BS}$  with daily MODIS data and in a time series of the MOD43B4 product. The analysis has also confirmed that soils can be spectrally differentiated from vegetation (regardless of vegetation photosynthetic status), by the relatively flat reflectance spectra in the SWIR region. This feature can be exploited using broadband multispectral sensors like MODIS for mapping vegetation fractional cover in mixed tree-grass ecosystems across the world.

### Our findings are:

1. Fractional cover of  $f_{PV}$ ,  $f_{NPV}$  and  $f_{BS}$  was quantified with hyperspectral data by calculating the NDVI and the CAI and applying a linear unmixing technique. Evidence from field and fire scar data showed that the results obtained reproduced the expected spatial and temporal patterns in savanna sites in northern Australia.
2. The ratio of MODIS bands SWIR3 and SWIR 2 (bands 7 and 6, 2200 nm and 1600 nm, respectively) was linearly correlated with the NDVI and CAI derived from Hyperion considered simultaneously. We

found that vegetation fractional cover can be successfully resolved with MODIS data by combining the SWIR3/SWIR2 ratio and NDVI.

3. As in any application of reflective remote sensing for vegetation monitoring in tropical regions, the presence of clouds constitutes a challenging issue. The use of 16-days composites (MODIS NBAR) partially solves this. In the case of the Australian tropical savannas, however, this is still problematic particularly during the monsoon season (November to April) when even with the compositing algorithm cloud-free data is not acquired.

## Acknowledgements

We thank Cate Ticehurst for her help with the atmospheric correction of Hyperion; Edward King and Matt Paget for providing assistance with the MODIS data; and Randall Donohue; Tim McVicar and Vittorio Brando for their useful comments in an early phase of manuscript preparation. This research was partially supported by the NASA Earth Science Enterprise Carbon Cycle Science research program (NRA04 OES-01). The Bushfire CRC provided funding for the curing measurements used in validation. The fractional cover derived from MODIS NBAR for the Australian savannas are available at <http://www-data.wron.csiro.au/remotesensing/> MODIS/products/Guerschman\_etal\_RSE2009.

## References

Anderson, S., Anderson, W., Hines, F., & Fountain, A. (2005). Determination of field sampling methods for the assessment of curing levels in grasslands. In Melbourne, Australia: Australian Bushfire Cooperative Research Centre-[www.bushfirecrc.com/research/downloads/Curing%20sampling%20methods%20final%20report.pdf](http://www.bushfirecrc.com/research/downloads/Curing%20sampling%20methods%20final%20report.pdf) Apan, A., & Held, A. (2002). In-House Workshop on Hyperion Data Processing. Echo-ing the Sugarcane Project Experience. Black Mountain Laboratories, Canberra: CSIRO Land and Water.

Apan, A., Held, A., Phinn, S., & Markley, J. (2004). Detecting sugarcane 'orange rust' disease using EO-1 Hyperion hyperspectral imagery. *International Journal of Remote Sensing*, 25, 489–498.

Asner, G. P., Borghi, C. E., & Ojeda, R. A. (2003). Desertification in Central Argentina: changes in ecosystem carbon and nitrogen from imaging spectroscopy. *Ecological Applications*, 13, 629–648.

Asner, G. P., Elmore, A. J., Hughes, R. F., Warner, A. S., & Vitousek, P. M. (2005). Ecosystem structure along bioclimatic gradients in Hawaii from imaging spectroscopy. *Remote Sensing of Environment*, 96, 497–508.

Asner, G. P., & Heidebrecht, K. B. (2003). Imaging spectroscopy for desertification studies: comparing AVIRIS and EO-1 Hyperion in Argentina drylands. *IEEE Transactions on Geoscience and Remote Sensing*, 41, 1283–1296.

Asner, G. P., Knapp, D. E., Cooper, A. N., Bustamante, M. M. C., Olander, L. P., & Heidebrecht, K. B. (2005). Ecosystem structure throughout the Brazilian amazon from Landsat observations and automated spectral unmixing (vol 9, art no 7, 2005). *Earth Interactions*, 9.

Asner, G. P., & Lobell, D. B. (2000). A biogeophysical approach for automated SWIR unmixing of soils and vegetation. *Remote Sensing of Environment*, 74, 99–112.

Asner, G. P., Nepstad, D., Cardinot, G., & Ray, D. (2004). Drought stress and carbon uptake in an Amazon forest measured with spaceborne imaging spectroscopy. *Proceedings of the National Academy of Sciences of the United States of America*, 101, 6039–6044.

Bastin, G. N., Ludwig, J. A., Eager, R. W., Liedloff, A. C., Anderson, R. T., & Cobiac, M. D. (2003). Vegetation changes in a semiarid tropical savanna, northern Australia: 1973–2002. *Rangeland Journal*, 25, 3–19.

Beringer, J., Hutley, L. B., Tapper, N. J., & Cernusak, L. A. (2007). Savanna fires and their impact on net ecosystem productivity in North Australia. *Global Change Biology*, 13, 990–1004.

Berry, S. L., & Roderick, M. L. (2002). Estimating mixtures of leaf functional types using continental-scale satellite and climatic data. *Global Ecology and Biogeography*, 11, 23–39.

Boardman, J. W., & Kruse, F. A. (1994). Automated spectral analysis – a geological example using AVIRIS data, North Grapevine mountains, Nevada. *Proceedings of the Tenth Thematic Conference on Geologic Remote Sensing – Exploration, Environment, and Engineering*, Vol. I. (pp. 1407–1418).

Chen, X. Y., Hutley, L. B., & Eamus, D. (2003). Carbon balance of a tropical savanna of northern Australia. *Oecologia*, 137, 405–416.

D'Odorico, P., Laio, F., & Ridolfi, L. (2006). A probabilistic analysis of fire-

induced treegrass coexistence in savannas. *American Naturalist*, 167, E79–E87.

Datt, B., McVicar, T. R., Van Niel, T. G., Jupp, D. L. B., & Pearlman, J. S. (2003). Preprocessing EO-1 Hyperion hyperspectral data to support the application of agricultural indexes. *IEEE Transactions on Geoscience and Remote Sensing*, 41, 1246–1259.

Daughtry, C. S. T. (2001). Discriminating crop residues from soil by shortwave infrared reflectance. *Agronomy Journal*, 93, 125–131.

Daughtry, C. S. T., Doraiswamy, P. C., Hunt, E. R., Stern, A. J., McMurtrey, J. E., & Prueger, J. H. (2006). Remote sensing of crop residue cover and soil tillage intensity. *Soil and Tillage Research*, 91, 101–108.

Daughtry, C. S. T., Hunt, E. R., Doraiswamy, P. C., & McMurtrey, J. E. (2005). Remote sensing the spatial distribution of crop residues. *Agronomy Journal*, 97, 864–871.

Donohue, R. J., McVicar, T. R., & Roderick, M. L. (2008). Climate-related changes in Australian vegetation cover as inferred from satellite observations, 1981–2006. *Global Change Biology*. doi:10.1111/j.1365-2486.2008.01746.x

Donohue, R. J., Roderick, M. L., & McVicar, T. R. (2008). Deriving consistent long-term vegetation information from AVHRR reflectance data using a cover-triangle-based framework. *Remote Sensing of Environment*, 112, 2938–2949.

Fox, I. D., Neldner, V. J., Wilson, G. W., Bannink, P. J., Wilson, B. A., Brocklehurst, P. S., et al. (2001). The Vegetation of the Australian Tropical Savannas (Scale 1:1,000,000). Environmental Protection Agency, Brisbane and the Cooperative Research Centre for Sustainable Development of Tropical Savannas, Darwin.

Galvao, L. S., Pizarro, M. A., & Epiphany, J. C. N. (2001). Variations in reflectance of tropical soils: spectral-chemical composition relationships from AVIRIS data. *Remote Sensing of Environment*, 75, 245–255.

Gill, T., & Phinn, S. (2008). Estimates of bare ground and vegetation cover from Advanced Spaceborne Thermal Emission and Reflection Radiometer (ASTER) shortwave-infrared reflectance imagery. *Journal of Applied Remote Sensing*, 2, 023511.

Gill, T., & Phinn, S. (2009). Improvements to ASTER-derived fractional estimates of bare ground in a Savanna Rangeland. *IEEE Transactions on Geoscience and Remote Sensing*, 47, 662–670.

Grace, J., San Jose, J., Meir, P., Miranda, H. S., & Montes, R. A. (2006). Productivity and carbon fluxes of tropical savannas. *Journal of Biogeography*, 33, 387–400.

Hill, M. J., Held, A. A., Leuning, R., Coops, N. C., Hughes, D., & Cleugh, H. A. (2006). MODIS spectral signals at a flux tower site: relationships with high-

resolution data, and CO2 flux and light use efficiency measurements. *Remote Sensing of Environment*, 103, 351–368.

Hill, M. J., Lesslie, R., Donohue, R. J., Houlder, P., Holloway, J., Smith, J., et al. (2006). Multi-criteria assessment of tensions in resource use at continental scale: a proof of concept with Australian rangelands. *Environmental Management*, 37, 712–731.

Hill, M. J., Roxburgh, S. H., Carter, J. O., & McKeon, G. M. (2005). Vegetation state change and consequent carbon dynamics in savanna woodlands of Australia in response to grazing, drought and fire: a scenario approach using 113 years of synthetic annual fire and grassland growth. *Australian Journal of Botany*, 53, 715–739.

Huete, A. R. (1988). A soil-adjusted vegetation index (SAVI). *Remote Sensing of Environment*, 25, 295–309.

Huete, A. R., Miura, T., & Gao, X. (2003). Land cover conversion and degradation analyses through coupled soil-plant biophysical parameters derived from hyperspectral EO-1 Hyperion. *IEEE Transactions on Geoscience and Remote Sensing*, 41, 1268–1276.

Ji, Y. M., & Stocker, E. (2002). Seasonal, intraseasonal, and interannual variability of global land fires and their effects on atmospheric aerosol distribution. *Journal of Geophysical Research-Atmospheres*, 107.

Jia, G. J., Burke, I. C., Goetz, A. F. H., Kaufmann, M. R., & Kindel, B. C. (2006). Assessing spatial patterns of forest fuel using AVIRIS data. *Remote Sensing of Environment*, 102, 318–327.

Jupp, D. L. B., Datt, B., Lovell, J., Campbell, S., & King, E. A. (2002). Discussion around Hyperion data: Background notes for the Hyperion Data Users Workshop Canberra Australia: CSIRO EOC.

Leuning, R., Cleugh, H. A., Zegelin, S. J., & Hughes, D. (2005). Carbon and water fluxes over a temperate Eucalyptus forest and a tropical wet/dry savanna in Australia: measurements and comparison with MODIS remote sensing estimates. *Agricultural and Forest Meteorology*, 129, 151–173.

Levy, E. B., & Madden, E. A. (1933). The point method of pasture analysis. *New Zealand Journal of Agriculture*, 45, 267–279.

Lobell, D. B., & Asner, G. P. (2002). Moisture effects on soil reflectance. *Soil Science Society of America Journal*, 66, 722–727.

Lobell, D. B., Asner, G. P., Law, B. E., & Treuhart, R. N. (2001). Subpixel canopy cover estimation of coniferous forests in Oregon using SWIR imaging spectrometry. *Journal of Geophysical Research-Atmospheres*, 106, 5151–5160.

Lu, H., Raupach, M. R., McVicar, T. R., & Barrett, D. J. (2003). Decomposition of vegetation cover into woody and herbaceous components using AVHRR NDVI time series. *Remote Sensing of Environment*, 86, 1–18.

Ludwig, J. A., Eager, R. W., Bastin, G. N., Chewings, V. H., & Liedloff, A. C. (2002). A leakiness index for assessing landscape function using remote sensing. *Landscape Ecology*, 17, 157–171.

Ludwig, J. A., Tongway, D. J., Bastin, G. N., & James, C. D. (2004). Monitoring ecological indicators of rangeland functional integrity and their relation to biodiversity at local to regional scales. *Austral Ecology*, 29, 108–120.

Ludwig, J. A., Wilcox, B. P., Breshears, D. D., Tongway, D. J., & Imeson, A. C. (2005). Vegetation patches and runoff-erosion as interacting ecohydrological processes in semiarid landscapes. *Ecology*, 86, 288–297.

Marsett, R. C., Qi, J. G., Heilman, P., Biedenbender, S. H., Watson, M. C., Amer, S., et al. (2006). Remote sensing for grassland management in the arid Southwest. *Rangeland Ecology and Management*, 59, 530–540.

McTainsh, G. H., Leys, J. F., Carter, D., Butler, H. J., McCord, A., Wain, A., et al. (2006). Monitoring soil condition across Australia: recommendations from the expert panels. Canberra, Australia: National Committee on Soil and Terrain for the National Land and Water Resources Audit.

Mistry, J. (2000). World savannas. *Ecology and Human Use* (pp. 1–25).

England: Pearson Education.

Miura, T., Huete, A. R., Ferreira, L. G., & Sano, E. E. (2003). Discrimination and biophysical characterization of cerrado physiognomies with EO-1 hyperspectral Hyperion. In XI Simposio Brasileiro de Sensoriamento Remoto – SBSR (pp. 1077–1082). Belo Horizonte, Brasil.

Nagler, P. L., Daughtry, C. S. T., & Goward, S. N. (2000). Plant litter and soil reflectance. *Remote Sensing of Environment*, 71, 207–215.

Nagler, P. L., Inoue, Y., Glenn, E. P., Russ, A. L., & Daughtry, C. S. T. (2003). Cellulose absorption index (CAI) to quantify mixed soil-plant litter scenes. *Remote Sensing of Environment*, 87, 310–325.

Numata, I., Roberts, D. A., Chadwick, O. A., Schimel, J., Sampaio, F. R., Leonidas, F. C., et al. (2007). Characterization of pasture biophysical properties and the impact of grazing intensity using remotely sensed data. *Remote Sensing of Environment*, 109, 314–327.

Okin, G. S. (2007). Relative spectral mixture analysis – a multitemporal index of total vegetation cover. *Remote Sensing of Environment*, 106, 467–479.

Olson, D. M., Dinerstein, E., Wikramanayake, E. D., Burgess, N. D., Powell, G. V. N., Underwood, E. C., et al. (2001). Terrestrial ecoregions of the world: a new map of life on Earth. *Bioscience*, 51, 933–938.

Paget, M. J., & King, E. A. (2008). MODIS Land data sets for the Australian region. CSIRO Marine and Atmospheric Research Internal Report No. 004 96pp, Available at [soils in AVIRIS data. \*Remote Sensing of Environment\*, 44, 255–269.

Scanlon, T. M., Caylor, K. K., Manfreda, S., Levin, S. A., & Rodriguez-Iturbe, I. \(2005\). Dynamic response of grass cover to rainfall variability: implications for the function and persistence of savanna ecosystems. \*Advances in Water Resources\*, 28, 291–302.

Schaaf, C. B., Gao, F., Strahler, A. H., Lucht, W., Li, X. W., Tsang, T., et al. \(2002\). First operational BRDF, albedo nadir reflectance products from MODIS. \*Remote Sensing of Environment\*, 83, 135–148.

Tucker, C. J. \(1979\). Red and photographic infrared linear combinations for monitoring vegetation. \*Remote Sensing of Environment\*, 8, 127–150.

Ustin, S. L., Roberts, D. A., Gamon, J. A., Asner, G. P., & Green, R. O. \(2004\). Using imaging spectroscopy to study ecosystem processes and properties. \*Bioscience\*, 54, 523–534.

Vermote, E. F., El Saleous, N. Z., & Justice, C. O. \(2002\). Atmospheric correction of MODIS data in the visible to middle infrared: first results. \*Remote Sensing of Environment\*, 83, 97–111.

Weidong, L., Baret, F., Xingfa, G., Qingxi, T., Lanfen, Z., & Bing, Z. \(2002\). Relating soil surface moisture to reflectance. \*Remote Sensing of Environment\*, 81, 238–246.](http://www-data.wron.csiro.au/rs/MODIS/LPDAAC/Palacios-Orueta, A., & Ustin, S. L. (1998). Remote sensing of soil properties in the Santa Monica Mountains I. Spectral analysis. Remote Sensing of Environment</i>, 65, 170–183. Ray, T. W., & Murray, B. C. (1996). Nonlinear spectral mixing in desert vegetation. <i>Remote Sensing of Environment</i>, 55, 59–64. Roberts, D. A., Smith, M. O., & Adams, J. B. (1993). Green vegetation, nonphotosynthetic vegetation, and</p></div><div data-bbox=)

Juan Pablo Guerschman <sup>a,\*</sup>, Michael J. Hill <sup>b</sup>, Luigi J. Renzullo <sup>a</sup>, Damian J. Barrett <sup>a,1</sup>, Alan S. Marks <sup>a</sup>, Elizabeth J. Botha <sup>a,c</sup>

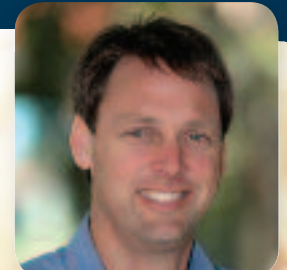
<sup>a</sup> CSIRO Land and Water, GPO Box 1666, Canberra, ACT 2601, Australia <sup>b</sup> Department of Earth Systems Science and Policy, University of North Dakota, Grand Forks, ND 58202, USA <sup>c</sup> Bushfire Cooperative Research Center



**YOUR COMPLETE AUSTRALIAN FARM ADVICE COMPANY**

Farmanco comprises 20 professional consultants providing independent advice to 750 farm businesses across Australia. Eric Nankivell (based in Albury, NSW) loves the farming industry and will challenge your business to remain progressive and profitable.

[www.farmanco.com.au](http://www.farmanco.com.au)



**Eric Nankivell**  
0428 914 263  
[enankivell@farmanco.com.au](mailto:enankivell@farmanco.com.au)